

# A novel device for a vertical rocking isolation system with uplift allowed for industrial equipment and structures

Sergio I. Reyes<sup>a,\*</sup>, José L. Almazán<sup>b</sup>

<sup>a</sup> Research Center for Integrated Disaster Risk Management (CIGIDEN), ANID/FONDAP/15110017, Pontificia Universidad Católica de Chile, Vicuña Mackenna 4860, Santiago, Chile

<sup>b</sup> Department of Structural and Geotechnical Engineering, Pontificia Universidad Católica de Chile, Vicuña Mackenna 4860, Santiago, Chile

## ARTICLE INFO

### Keywords:

ISO3D-2G device  
Three-dimensional seismic isolation  
Vibration isolation  
Industrial equipment  
Hyperelasticity  
Rocking behavior

## ABSTRACT

In this paper, a novel device called the “ISO3D-2G” is proposed for a three-dimensional vertical rocking isolation (VRI) system. The VRI system works by isolating critical vibration sources, e.g., earthquake events and operational high-frequency vibrations. In this work, only its performance as a seismic isolation system is studied. The ISO3D-2G is made of a steel structure and an elastomeric rubber system, offering improved properties as compared to previous versions of the device. The device is manufactured at a full scale and is experimentally tested. To represent the vertical non-linear hysteretic behavior of the device, a numerical model called the hyperelastic Bouc-Wen (HBW) model is developed. The HBW model combines a hyperelastic component (represented in this work by a third-order Ogden model) and a hysteretic component (represented by a modified BW model). The simply supported horizontal behavior of the device is represented through a non-linear 2D frictional hysteretic model. The HBW model is calibrated to fit the experimental data obtained in the test, and guidelines are provided for understanding and manually calibrating the model. The dynamic performance of the system is analyzed using time-history analyses with four records (three non-impulsive records and one impulsive record). Equations are presented for the motion of the system. For the three non-impulsive seismic records, the observed behavior was similar to that in conventional lateral isolation systems. Horizontal force reduction ratios between 7.4 and 10.9 were obtained. The maximum shear base remained below 23% of the total weight of the structure, even considering the three components of the ground motion. In addition, vertical force reduction ratios between 2 and 3.8 were obtained, demonstrating that the vertical isolation effect was satisfactory. However, for an impulsive seismic record, there was a significant change in the patterns of behavior, owing to the significant uplift of two of the four devices. Despite this, the structure remained stable, and the lateral isolation effect was preserved. Finally, it was concluded that using vertically flexible devices with high damping in the base of structures to generate a rocking isolation mechanism is an effective approach to reducing the seismic demand, even though the isolated modes of the structure do not take periods longer than 2.0 s. Although there was no lateral translation at the base, the VRI system isolated the structure by allowing lateral and vertical displacement of the center of mass.

## 1. Introduction

Over the last five decades, several seismic isolation systems have been studied and developed worldwide. Most of them provide a structure for lateral isolation, similar to approaches with elastomeric or frictional devices. However, in these devices, the vertical component of the seismic motion is still transmitted directly into the structure. Vertical isolation is needed for two main purposes: (i) to reduce damaging vertical ground accelerations from earthquakes that are transmitted to the structure, causing a reduction in the shear and flexural

capacity of the supporting elements [1–4]; and (ii) to reduce the vertical high-frequency operational vibrations of industrial equipment that must comply with serviceability objectives, as they also could cause damage to the environment (e.g., near people working, other important machinery, or non-structural completion of the building) [5]. However, the existing solutions for operational high-frequency vibrations (vibration control devices) do not have good performance in response to seismic events [6,7]. Hence, vertical isolation is needed to protect structures, especially structures with failure modes associated with vertical seismic components.

\* Corresponding author.

E-mail addresses: [sergio.reyes@cigiden.cl](mailto:sergio.reyes@cigiden.cl) (S.I. Reyes), [jlalmaz@ing.puc.cl](mailto:jlalmaz@ing.puc.cl) (J.L. Almazán).

<https://doi.org/10.1016/j.engstruct.2020.110595>

Received 28 March 2019; Received in revised form 24 March 2020; Accepted 30 March 2020

Available online 18 April 2020

0141-0296/ © 2020 Elsevier Ltd. All rights reserved.

Three-dimensional seismic isolation systems (3DSISs) have been recently studied for providing horizontal and vertical isolation. These systems usually allow six vibration modes: three lateral-torsional modes and three vertical-rocking modes, i.e., similar to the concept of isolation in industrial equipment. For example, the application of a three-dimensional seismic isolation bearing system in long-span hangars was analyzed by Xiongyan et al [8]; Xu et al. [9,10] designed and tested a multi-dimensional isolation device for building structures; Takahashi et al [11] proposed a 3DSIS with a rocking suppression system for an entire civilian building; Blom [12] studied the vertical and horizontal seismic isolation performances of an advanced virgo external injection bench seismic attenuation system. In addition, 3DSISs for nuclear power plants have been exhaustively analyzed. These protect the structure itself, along with specialized equipment and machinery that is not only expensive, but critical to safe operation [13–16].

The same concept of seismic protection can be applied to specialized equipment that is critical for operational continuity. Most seismic design codes are guidelines for engineers in regard to requirements and/or criteria for life safety in buildings. However, in the case of industrial facilities, these requirements are not sufficient to ensure the safety of assets and essential machinery that must be operational following an earthquake. Considering that some of these critical structures include motorized mechanical equipment that produces high-frequency vibration under regular daily operation, there is great value in determining a cost-effective retrofitting solution for simultaneous vibration control and seismic protection.

An example of a 3DSIS available in the market and used for seismic protection and isolating excessive or disturbing vibrations is the GERB base control system device. It consists of a set of compression springs and viscous dampers placed at the bottom of the structure, and been applied in different fields, such as building isolation, industrial machinery, pipework systems, and shipbuilding [17]. Another three-dimensional isolation system is a vertical rocking isolation (VRI) system. It was first proposed by Almazán et al. [18] as a viable alternative for seismically protecting legged wine storage tanks, inspired by the benefits of the rocking motions of structures. Other protection devices that take advantage of the rocking behavior of structures have also been proposed. For example, Alessandri et al. [19,20] analyzed the seismic protection of electrical substation equipment by using wire rope devices as rocking isolation mechanisms. Friction spring dampers [21] were studied as a rocking energy-dissipation mechanism by Riley et al. [22]. Generally, rocking-based protection systems have been shown to be particularly effective for slender structures.

The first materialization of a VRI system was through a device called the “ISO3D” [23]. García G. [24] analyzed the performance of the VRI system in the seismic isolation of 12 tons of air conditioning equipment supported by four ISO3D devices. He concluded that the main

contribution of this technology, as compared to traditional vibration control devices, is the reduction in the acceleration response of the equipment to high-intensity earthquakes. He presented an effective alternative for protecting these structures, as the performances of heavy and light equipment supported by vibration control devices have been deficient in many earthquakes, showing failures in anchorages, and damage in acceleration-sensitive components [25].

The 2010 Maule Earthquake led to the study of the seismic performance of many vulnerable structures. One study addressed legged wine storage tanks, and was triggered by the economic losses to the wine industry from that event [26]. Similar damage scenarios occurred in other seismic countries, e.g., in the 2012 Emilia Earthquake in Italy [27], 2011 Christchurch and 2013 Marlborough Earthquakes in New Zealand [28], 2014 South Napa Earthquake in the USA [29], and 2015 Coquimbo Earthquake in Chile (again). In all of these events, the winery industries were harshly affected. This demonstrated that seismic protection was necessary for wine storage systems, just like any other important asset. Thus, Auad and Almazán [30] conducted a further study on the performance of the ISO3D in isolating a legged wine storage tank. They obtained significant compression and shear load reductions in the legs, which are the critical forces in commonly seen leg-buckling failures.

In this study, an improved version of the ISO3D device is developed, and is denoted as the “ISO3D-2G”. This version is the result of important changes made to the ISO3D device to obtain a better seismic response and a higher mass capacity, making it suitable for a larger number of light and heavy structures. Although the device is designed to work simultaneously as a seismic and vibration isolator, only its operation as a seismic isolator is validated herein. To validate its operation as a vibration isolator, further experimental studies are required.

## 2. Description of the isolation device ISO3D-2G

The essence of the ISO3D-2G is to unify the well-known concepts of vibration control (in industrial equipment) and seismic isolation in a unique device. The main changes made to the ISO3D include: (i) the addition of a central solid rod that restrains the lateral displacement; (ii) the replacement of all steel springs by high-damping rubber bearings (HDRBs), and (iii) the removal of the internal energy damper. The replacement of the steel springs is mainly because the HDRBs have a highly non-linear hysteretic force-deformation relation that is more suitable for seismic isolation than linear elastic springs.

Thus, the ISO3D-2G consists mainly of four parts: (i) an articulated framework structure, (ii) a compression and tension rubber bearings, (iii) a central rod, and (iv) a support structure. Fig. 1a shows an isometric view of the device in an undeformed configuration, and the

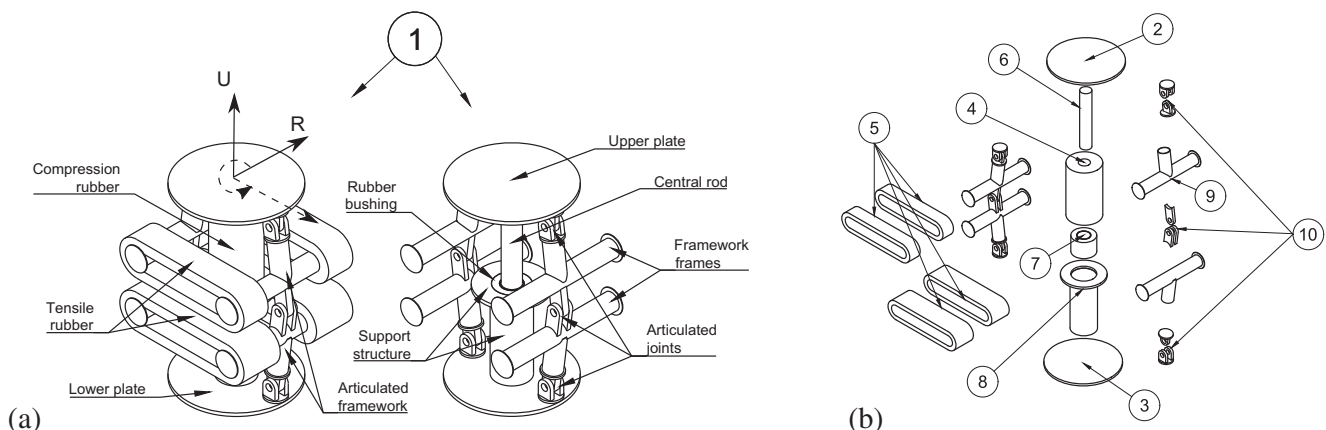


Fig. 1. (a) Isometric view of the ISO3D-2G, with and without rubber bearings; (b) exploded view of the components.

**Table 1**  
Components in Fig. 1b.

N°	Element	N°	Element
1	ISO3D-2G device	6	Central rod
2	Upper plate	7	Rubber bushing
3	Lower plate	8	Support structure
4	Compression rubber	9	Framework frames
5	Tensile rubber	10	Articulated joints

name of each component. An exploded view of the components is presented in Fig. 1b. Table 1 presents the generic name of each numbered component.

The articulated framework is responsible for transferring and amplifying the vertical deformation(s) to the horizontal rubber bands. It consists of an upper plate (element N° 2) connected to the structure, a lower plate (element N° 3) in contact with the floor, and four frames (element N° 9) where the horizontal rubber bands are attached. All components are connected through articulated joints (element N° 10), forming a hexagonal frame. In the ISO3D device, this framework was made of six robust plates, to resist all of the lateral forces in one direction. However, when these forces are too high (e.g., associated with heavier structures), the design results in excessively thick and complex plate connections. To solve this problem, the central rod (element N° 6) was added to resist the lateral forces instead of the framework; thus, the plates could be replaced by thinner frames.

The compression rubber (element N° 4) provides the flexibility for isolation from external vibrations; the tensile rubber (element N° 5) reduces the deformation caused by the self-weight of the structure, and provides additional energy dissipation. The compression rubber is placed between the support structure (element N° 8) and the upper plate of the framework. The compression rubber includes a hole in the middle for the central rod to pass through. The tensile rubbers are attached to the framework structure. Although the compression and

tensile rubbers perform different functions, according to the desired behavior, only compression rubbers can be used in the design to reduce costs, provided larger self-weight deformations are acceptable.

The central rod resists lateral forces and avoids the buckling of the compression rubber. It also works as a guideline for the vertical movement of the device. It is connected to the upper plate of the framework and passes through a flexible annular bushing (element N° 7) placed in the support structure. The bushing guides the vertical movement of the rod, and allows the rotation of the upper plate. Owing to the nearly incompressible behavior of rubber, when the compression rubber is deformed, it tends to expand laterally but also inwards, owing to the hole in the middle. Accordingly, it confines the central rod, and dissipates energy via friction.

The support structure is where the compression rubber rests and has a fundamental role in the design of the system. It regulates the height of the device and modifies the amplification effect of the framework structure. Importantly, the flexible annular bushing manages to match, at least with an acceptable tolerance, the equivalent lateral stiffness of all devices when they have different levels of deformation (e.g., vertical deformation changes the free length of the rod, and thus the lateral stiffness).

As mentioned before, the articulated framework transfers and amplifies the vertical deformation of the device to the horizontal rubber through a kinematic relation. By applying the virtual work principle to this relation, the vertical non-linear vertical force  $f_u$  provided by any rubber spring on the device and its corresponding tangent stiffness  $k_u$  can be determined as follows:

$$f_u = (f_s + f_o) \frac{\partial s}{\partial u} \quad (1)$$

In the above,  $u$  is the vertical deformation of the device;  $s$  and  $f_s$  are the uniaxial deformation and the force of the rubber spring, respectively, and  $f_o$  is the pre-stressing load in the rubber (if any). In the case of the compression rubber, the term  $\frac{\partial s}{\partial u}$  is equal to 1, because the vertical

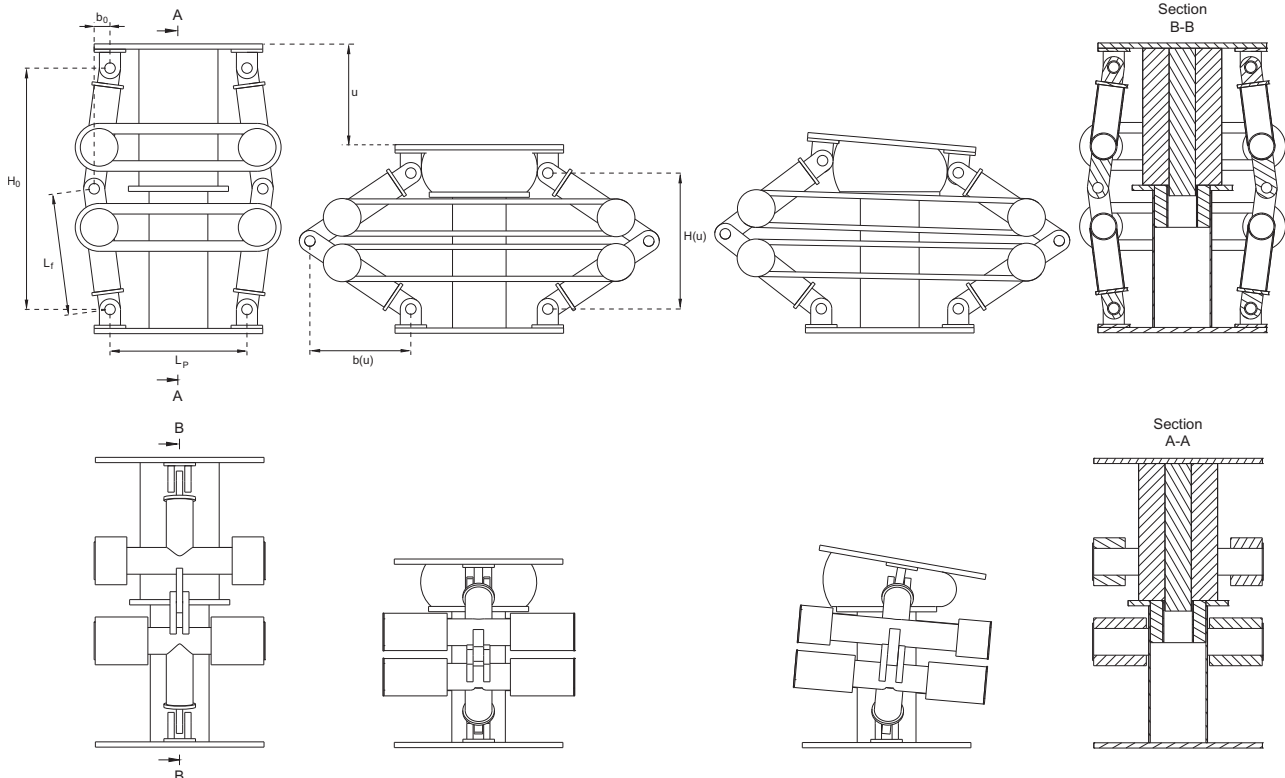


**Fig. 2.** From left to right, the two main orthogonal views of the device in the undeformed position, vertically deformed position, vertically deformed position with a slight rotation, and a view of the cross sections.

deformation of the rubber coincides with that of the device. In in the case of tensile rubber bands, the term  $\frac{\partial s}{\partial u}$  depends on the geometry of the hexagonal framework, as the amplification effect lies there. Fig. 2 shows the main orthogonal views of the device in the undeformed position and in a vertically deformed position with a slight rotation, along with cross-sectional views. From this figure, it is possible to observe and better understand the kinematics of the device.

### 2.1. Prototype tests

As mentioned previously, the restitutive force of the ISO3D-2G device is provided by the rubber, under uniaxial compression and tension. Rubber has been used as an engineering material for almost 200 years, i.e., since the vulcanization of rubber as pioneered by Charles Goodyear. Since then, its mechanical properties have been modified for different purposes. Generally, these properties are strongly modified by adding fillers (silica or carbon black) that create new bonds between the polymer and filler particles [31–33]. Filled rubbers are strongly characterized by a stress-softening behavior under cyclic uniaxial deformation; this effect was intensively investigated by Mullins and his co-workers, and was referred to as the “Mullins effect” [34–38]. This stress-softening effect is also widely known as “scragging”, and its effect has also been extensively studied in high-damping rubber bearings under shear deformations [39–41].

To validate the improvements made to the ISO3D device, four identical prototypes of the ISO3D-2G device were manufactured for laboratory testing. The devices were designed to support 0.8 Tonf under a self-weight condition. Therefore, with four devices, it is possible to support a structure with an approximate weight of 3.2 Tonf. The framework structure of the devices comprised ASTM A36 steel with an electrolytic zinc plating finish. The compression and tensile rubber were manufactured from natural rubber, with a hardness of Shore 70 (scale type A, measured with quadrant-style durometer), and a tensile rupture strain of 480% in uniaxial tension. The manufacturer did not provide information on the specific compositions of the rubber or its fillers; however, it is the same rubber used by the supplier to manufacture rubber bearings, bridge supports, and spring fenders. The dimensions of the framework structure and rubbers are presented in Table 2. To facilitate the manual installation of the rubbers and easily modify the amount of rubber to be used, each tensile rubber was manufactured as a unitary band with a 1 cm<sup>2</sup> cross-sectional area. In the tested device, 28 rubber bands were used.

## 3. Experimental setup and instrumentation

The device was tested at the Pontificia Universidad Católica de Chile Laboratory. A 90 kN capacity dynamic actuator with a servo valve was used as a loading device. It was anchored horizontally to a reaction wall and was held vertically using sensors. The device was tested horizontally between the dynamic actuator and a stiff-reaction metallic bracket

**Table 2**  
Dimensions of the device.

Notation	Dimension
Initial height of device, $H_0$	250 mm
Initial opening of the framework, $b_0$	25 mm
Length of each frame, $L_f$	120 mm
Separation width of the framework, $L_p$	100 mm
Tensile rubber initial length, $L_t$	160 mm
Height of compression rubber, $h_c$	125 mm
External diameter of the compression rubber, $D_e$	80 mm
Internal diameter of the compression rubber and diameter of the central rod, $D_i$	30 mm
Number of tensile rubber bands	28
Initial cross-sectional area of compression rubber	43.2 cm <sup>2</sup>
Initial cross-sectional area of each tensile rubber	1 cm <sup>2</sup>

anchored to the reaction slab of the laboratory. A linear variable differential transformer with a 150 mm stroke length was installed to measure the applied displacement on the upper plate of the device. A 50 kN capacity tension-compression load cell was placed between the device and the dynamic actuator to measure the applied force. Fig. 3 presents a photograph and layout of the experimental setup.

### 3.1. Testing protocol

Several regulations propose tests for isolation devices, which are intended to verify the device performance under a wide range of loads and displacements [42]. However, it was decided to apply the vertical three-phase displacement pattern shown in Fig. 4 instead (vertical displacement considering the local axes of the device). This pattern was chosen to observe three phenomena in the elastomers: (a) the stiffness degradation owing to the Mullins effect in the loading and unloading curves at different levels of deformation, (b) the unloading curve path at different levels of deformation, and (c) the hysteretic cyclic behavior at a deformation equal to half of the design deformation, to thereby adjust a numerical model. The design deformation corresponded to the maximum expected deformation for the designed earthquake, i.e., a deformation of 50% in the compression rubber. For the authors, the latter was the most interesting phenomenon represented through the applied protocol.

Each phase of the protocol showed a specific behavior of the elastomers. The first phase produced scragging in the virgin rubber at different levels of deformation until it reached the design deformation, to thereby compare the stress-softened curves in the following phases. The second phase obtained the hysteretic cyclic behavior centered at half of the design deformation, as that would be the predominant hysteretic behavior during an earthquake. Finally, the third phase obtained the stress-softened loading and unloading curve paths for different levels of deformation, to determine if a significant loss of stiffness persisted.

Each cycle was performed at a constant frequency of 0.33 Hz. The largest amplitude reached a deformation of 68 mm. Phase 2 was centered on a deformation of 35 mm (approximately half of the design deformation). With these peak displacement amplitudes, the rubber was subjected to a range of strain rates from approximately 0.05 s<sup>-1</sup> to 0.4 s<sup>-1</sup> in the first and last cycles of phase 1, respectively.

Although the ultimate capacity of the device was estimated to be approximately 80–90 mm of deformation in the compression rubber (failure by yield of the device's support structure), the applied deformation was limited to the design level, to maintain the device in working condition and ready for installation in a storage tank (for an ongoing full-scale shaking table test validation).

To certify the use of these devices for the seismic protection of specific equipment for commercial purposes, other more rigorous displacement patterns may be required before installation. For example, for the protection of electrical equipment in substations, it is necessary to comply with the test protocol established in t Appendix W of the IEEE Standard 693-2018: “Recommended Practice for Seismic Design of Substations,” which has specific recommendations for devices that use a rocking isolation mechanism [43].

### 3.2. Test results

Three of the prototypes (referred to as prototypes A, B, and C) were tested with different rubber configurations to analyze the contributions of elastomers in compression and tension (separately). Prototype A was tested with only non-virgin compression rubber (i.e., rubber that was already deformed, so no important scragging is present), prototype B was tested with only virgin tensile rubbers, and prototype C was tested with both rubber systems (non-virgin compression rubber and virgin tensile rubbers). Unfortunately, at the initial testing of the compression rubbers in their virgin state, there was an error in the instrumentation, and those data are not available. That is why the compression rubber

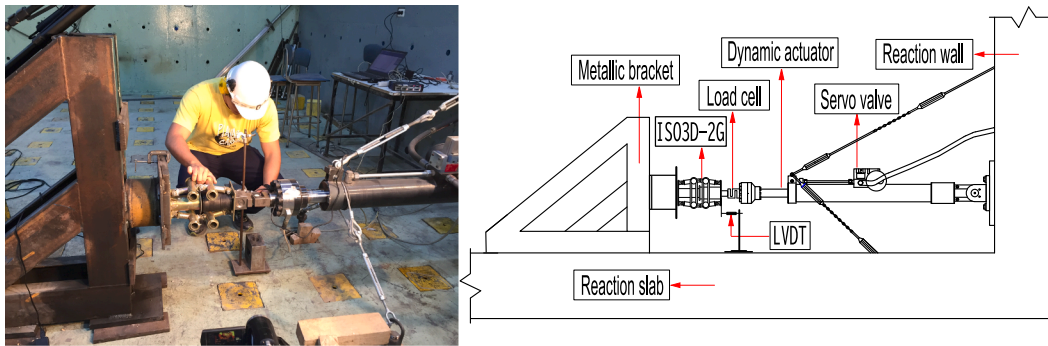


Fig. 3. Experimental setup.

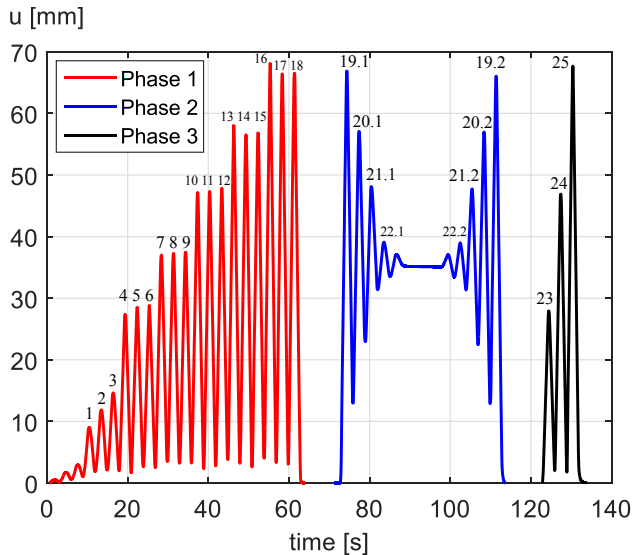


Fig. 4. Applied vertical three-phase displacement pattern.

does not present a stiffness degradation in the initial cycles. It is important to mention that the steel framework structure is completely identical in the three prototypes. The force-deformation hysteretic loops measured during the tests for the three prototypes are shown in Fig. 5.

Although a fictitious primary curve can be clearly recognized in each test with virgin rubber, there is an important softening in the initial cycles. This softening effect cannot be neglected and should be considered in the design, as all devices must be tested at the maximum deformation before installation, assuring that there will be a stress-softening effect (as is applied to rubber bearing isolators through the scragging process). However, an interesting trend of these materials is that for numerous deformation cycles at deformation levels progressively smaller than the largest level reached before, a unique softened loading and unloading curve can be clearly identified, unless the last largest deformation is exceeded. This trend is evident in prototype A (with only compression rubber). As it was previously tested, the stress softening had already occurred, and all subsequently recorded loading and unloading curves went through the same path. The same behavior is observed in prototypes B and C in the final cycles of the test.

Table 3 presents the amplitude, effective stiffness ( $K_{eff}$ ), dissipated energy ( $E_d$ ), and equivalent linear viscous damping ratio ( $\xi$ ) of the hysteretic cycles for prototype C (the numeration of cycles refers to that shown in Fig. 4). Cycles with similar maximum deformation levels were separated using horizontal sublines (every three cycles in phases 1 and 3, and every two cycles in phase 2). The effective stiffness was computed as the slope between the maximum and minimum deformation values in a given cycle.

To quickly quantify the amount of energy dissipated for different levels of deformation (for use in design procedures, e.g., the capacity-demand method), a power function was adjusted to the experimental results in a least-square fitting sense. Fig. 6a shows the energy dissipated by prototype C as a function of the amplitude of the applied deformation cycles. The first cycles for a given deformation level during phase 1 were not considered in the fitting, as scragging must occur first. The not-considered cycles are shown in the graph as “Phase 1 (first cycles)” (i.e., cycles 1, 2, 3, 4, 7, 10, 13, and 16, referring to the numeration of Fig. 4). In contrast, all cycles of phases 2 and 3 were considered. According to the fitting, the energy dissipated in a fully reversed cycle of amplitude  $\Delta u$  is given as follows:

$$E_d(\Delta u) = 0.054 \cdot \Delta u^{1.484} [\text{Tonf} - \text{mm}] \quad (2)$$

Fig. 6b presents the relative error between the polynomial fitting and the experimental test values. Although there is a larger error for small amplitudes, these deformation amplitudes are not relevant for seismic applications, as the expected demand levels will be at amplitudes greater than 20 mm.

As to be expected in phase 1 owing to the scragging, the first cycle at a given deformation level has a larger amount of dissipated energy and stiffness than the two following cycles at that same deformation level. In the case of equivalent viscous damping, the same trend is observed for small deformation levels (amplitudes smaller than 30 mm), whereas for larger deformation levels, no relevant change is observed. Fig. 7 shows the effective stiffness values and equivalent linear viscous damping ratios of the cycles as a function of amplitude. It is observed that for deformation levels associated with seismic demands (amplitudes larger than 30 mm), the stiffness of the device remains reasonably constant. In addition, the equivalent damping slightly decreases as the deformation increases.

As shown by the previous results, the ISO3D-2G device has an energy dissipation capacity that allows for its use as a seismic isolator. Therefore, it is not necessary to incorporate other sources of dissipation (as additional dampers), resulting in a more cost-efficient design. This also overlooks the fact that in some cases, rubber bearings are cheaper than steel springs.

Based on the experimental results shown in this chapter, a hysterical model is presented below, to represent the vertical force-displacement relationship of the ISO3D-2G device.

#### 4. Vertical constitutive relations of the ISO3D-2G device

Unlike other materials, representing the mechanical behavior of rubber through a constitutive relation is very complex [44]. Although different dynamic models for rubber have been widely studied in elastomeric isolator devices [45–48], they only consider shear deformation, and not the uniaxial compression or tension behavior. In regards to the uniaxial cyclic deformation in filled rubbers, some models have been proposed to represent the Mullins effect [49–53], but are mainly focused on fitting the experimental test data with well-

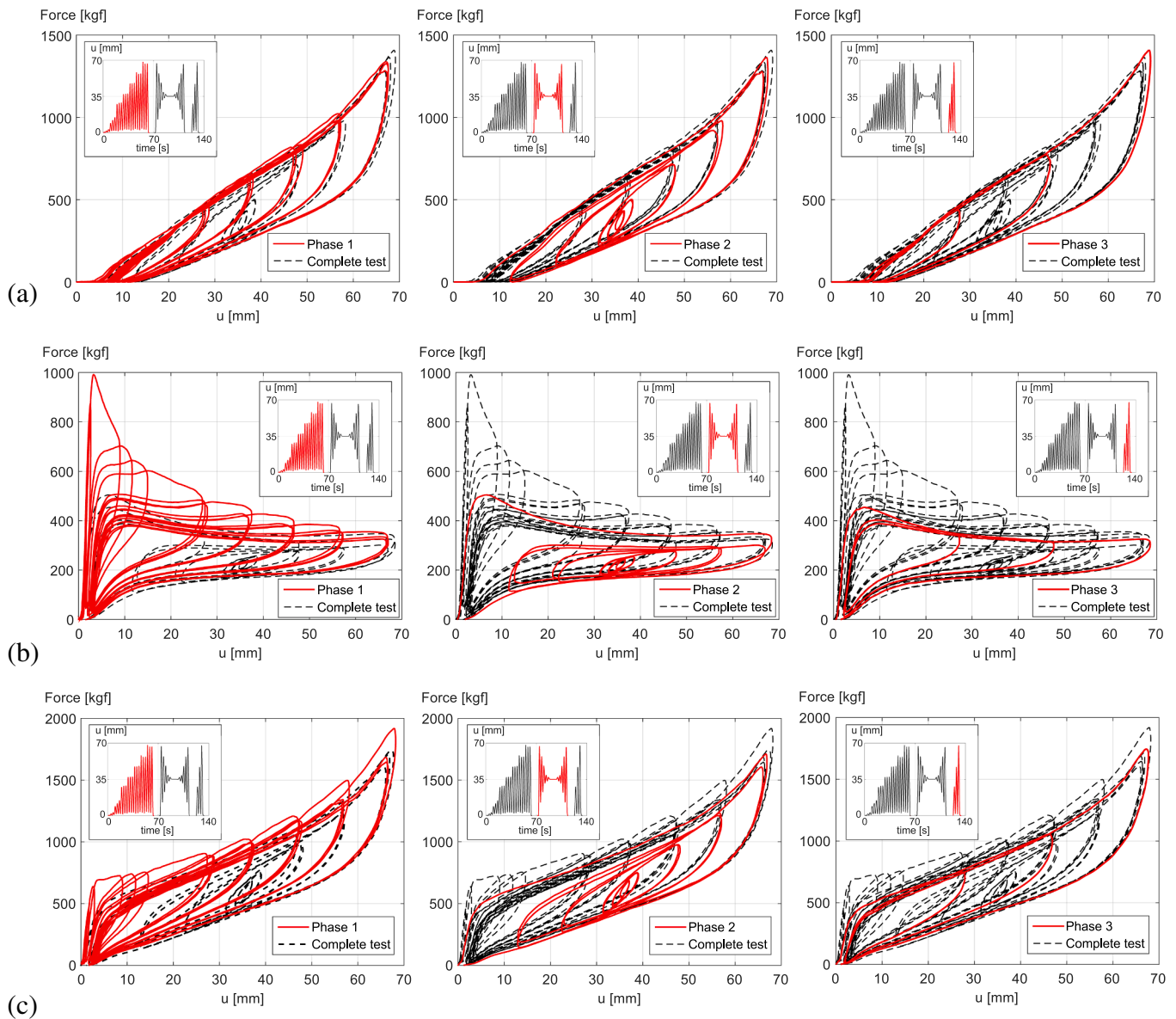


Fig. 5. Vertical force-deformation of: (a) prototype A (contribution of compression rubber), (b) prototype B (contribution of tensile rubber), and (c) prototype C (overall contribution of tensile and compression rubber).

known and controlled loading and unloading parameters. Even if the Mullins effect is neglected and a softened backbone curve is considered, the use of these models in time history analyses is complicated, as some cases of loading or unloading are not well-defined for different levels of deformation.

One of the most complete and available models for representing rubber behavior under uniaxial cyclic deformation was presented in a study by Rickaby et al. [54]. This model is capable of representing inelastic features including the Mullins effect, hysteresis, stress relaxation, residual strain, and creep of residual strain. Although Rickaby's model can adequately represent the measured behavior in phases 1 and 3, it cannot represent the behavior of phase 2, because the loading and unloading at the intermediate deformations are not defined. As such, discontinuous jumps are produced between the loading and unloading curves. This represents a major limitation, as phase 2 of the testing protocol comprises the most relevant behavior for a time-history analysis.

Although the Mullins effect is indeed essential in the behavior of rubber-like materials (as the ISO3D-2G devices will be tested and scragged to the maximum deformation before installation), no

significant softening effect is expected during earthquakes. Therefore, it is possible to consider stable hysteretic cycles in the modeling of the device.

Other rubber phenomena, such as relaxation and creep, are not expected to have a significant effect on the device. The relaxation effect of rubber after a scragging process is independent of both the applied strain and previous maximum strain, and remains as a constant fraction of the stress relaxed. It is unaffected by any preparatory scragging procedures [55]. This implies that scragging can be safely used to control the softening and modulus of the rubber, without affecting the relaxation process. Although some studies have shown that the relaxation effect of rubber may be neglected for the tested loads and deformation levels, it is essential to conduct further studies to accurately quantify its effects. The unrelaxed stress is expected to be nearly 95% for the considered strain deformation levels; [55] therefore, it is neglected in the modeling of the device.

Based on the above considerations, a novel model called the hyperelastic Bouc-Wen (HBW) model is developed for representing the vertical force-deformation relations of the ISO3D-2G device. As seen in Fig. 8, the HBW model comprises a modification of the BW model for

**Table 3**  
Properties of hysteretic cycles obtained for prototype C.

# Phase	# Cycle	$F_{max}$ [kgf]	$F_{min}$ [kgf]	$D_{max}$ [mm]	$D_{min}$ [mm]	Amplitude [mm]	$K_{eff}$ [kgf/mm]	$E_d$ [tonf-mm]	$\xi_{eff}$ [%]
Phase 1	1	658	52.3	9.0	1.0	8.0	76.0	3.2	41.5
	2	679	96.8	11.8	1.9	9.9	58.5	3.2	35.0
	3	700	41.7	14.6	2.0	12.6	52.3	3.8	29.6
	4	850	20.6	27.3	1.7	25.6	32.3	9.1	27.2
	5	865	25.2	28.6	1.7	26.9	31.2	8.0	22.6
	6	838	51.3	28.9	2.5	26.4	29.9	7.5	23.0
	7	965	69.8	37.0	2.5	34.5	26.0	11.4	23.6
	8	964	66.9	37.3	3.3	34.0	26.3	10.3	21.4
	9	953	78.7	37.4	3.3	34.1	25.6	10.3	22.0
	10	1131	30.2	47.2	2.3	44.9	24.6	15.5	20.0
	11	1133	39.0	47.4	2.3	45.1	24.3	15.0	19.4
	12	1142	54.9	47.8	2.8	45.0	24.1	14.9	19.3
	13	1407	68.0	58.1	3.2	54.9	24.4	21.3	18.4
	14	1290	30.4	56.5	2.6	53.9	23.4	19.2	18.0
	15	1292	51.0	56.9	2.6	54.3	22.9	19.6	18.5
	16	1806	56.3	68.2	3.3	64.9	27.0	28.5	16.0
	17	1604	41.5	66.4	3.0	63.4	24.7	25.5	16.4
	18	1582	12.8	66.6	3.0	63.6	24.7	25.3	16.1
Phase 2	19.1	1658	229.3	66.9	13.0	53.9	26.5	22.2	18.4
	19.2	1549	189.4	66	12.9	53.1	25.6	19.2	16.9
	20.1	1154	348.5	57.1	23.0	34.1	23.6	9.6	22.3
	20.2	1188	307.9	57.0	22.5	34.5	25.5	9.6	20.0
	21.1	937	464.7	48.1	31.4	16.7	28.4	3.4	27.8
	21.2	939	429.6	47.7	31.4	16.3	31.2	3.1	23.5
	22.1	733	515.7	39.1	33.5	5.6	39.3	0.5	24.7
	22.2	740	485.8	38.9	33.4	5.5	46.3	0.5	23.4
Phase 3	23	714	0	27.9	0.0	27.9	25.5	8.1	25.7
	24	1007	9.6	46.9	1.8	45.1	22.1	14.7	20.8
	25	1679	6.4	67.7	1.7	66.0	25.4	27.2	15.7

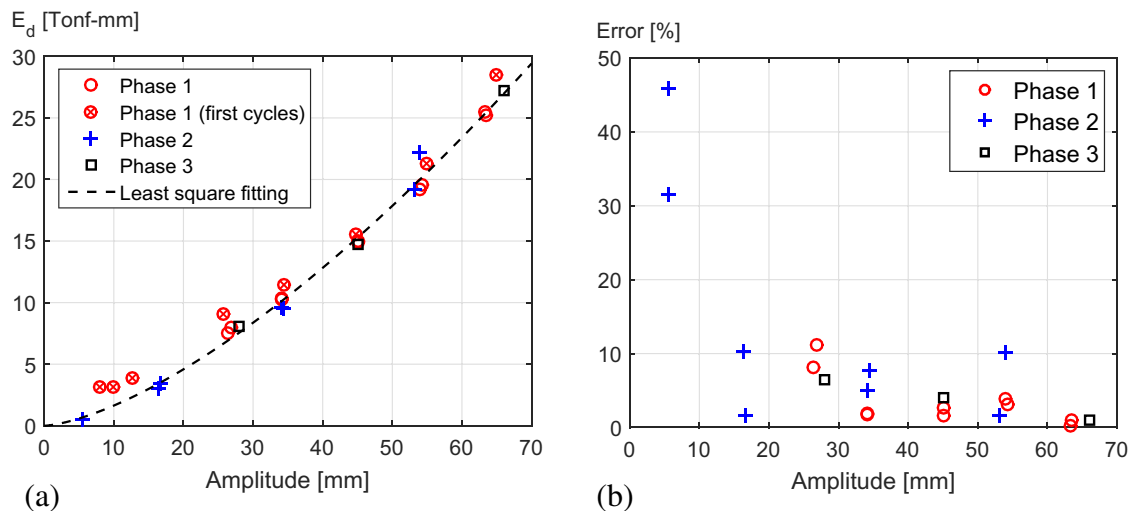


**Fig. 6.** (a) Dissipated energy by prototype C, (b) Relative error between the experimental results values and the fitting.

highly asymmetric hysteresis, connected in parallel to a nonlinear hyperelastic spring. This approach has also been used in other studies. For example, Osgoee et al. [56] proposed a pivot-elastic model for representing the lateral behavior of fiber-reinforced elastomeric isolators, and Alessandri et al. [19] modeled the behavior of wire rope isolators. However, no model has been proposed to represent the uniaxial behavior of elastomers under compression or tension for seismic purposes.

According to the HBW model, the force-deformation relation of the rubber under uniaxial deformation is given as follows:

$$F_v(u, Z) = f_{hyp} + f_{hys} = f(u)C_1 + (f(u)C_2^\phi + C_3^\phi)Z \quad (3)$$

Here,  $f_{hyp} = f(u)C_1$  is the nonlinear hyperelastic force, with  $f(u)$  being the monotonic force obtained after eliminating the scragging effect;  $f_{hys} = (f(u)C_2^\phi + C_3^\phi)Z$  is the hysteretic force, with  $Z$  as the internal hysteretic variable; and  $C_1$ ,  $C_2^\phi$ , and  $C_3^\phi$  are constant parameters, where

the superscript  $\phi$  denotes different values for representing asymmetric hysteresis according to the sign of  $Z$ .

A comparison between the experimental measures and numerical results for each phase of the testing protocol is shown in Fig. 9. The compression and tensile rubber are shown separately, and the latter is also shown with the kinematic amplification of the framework reversed. The criteria for the adjustment of the model was to match the amount of energy dissipated by the hysteretic cycles, as grouped by each phase of the testing protocol. Table 4 presents the relative error between the experimental tests and the calibrated model.

It is observed that the calibration of the compression rubber fit better to the tests than the tensile rubber, with a relative error of less than 2%. The larger relative error obtained in the tensile rubber might be because the model was not directly calibrated with raw experimental results; rather, the inverse kinematics of the framework had to be

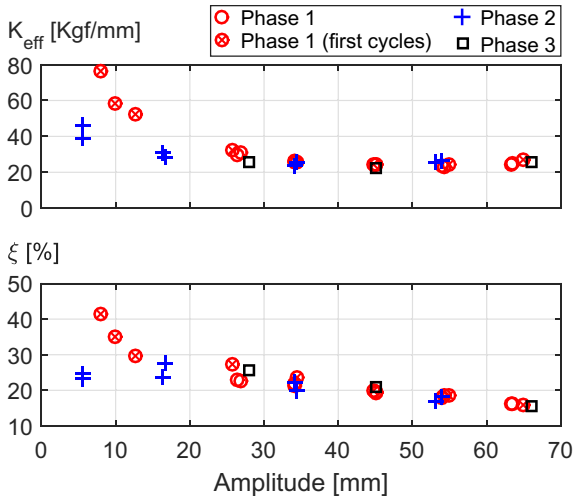


Fig. 7. Effective stiffness and equivalent linear viscous damping ratio of the device.

applied to obtain the uniaxial deformation of the tensile rubber. As a theoretical kinematic amplification was used according to Eq. (1) and the dimensions of the framework, the real amplification effect during the test may be slightly different from that obtained theoretically. In addition, the tensile rubber has a significant error in phase 1, as the model is not able to represent the Mullins effect that occurs in the first cycles.

The following subsections elaborate on the equations that represent the HBW model, and the methodology used to calibrate its parameters.

#### 4.1. Hyperelastic component

Models based on the theory of hyperelasticity are widely used to represent the mechanical behaviors of biological tissues, elastomers, foams, and rubber-like materials. In this theory, the models are derived from a strain-energy function  $W$ . Depending on the approach being

followed, two types of formulations mainly exist: (i) phenomenological models, which are mathematical developments of the function  $W$  (e.g., Mooney-Rivlin, Ogden), and (ii) physical models based on the spatial arrangement of the polymer chains network and statistical methods (e.g., eight-chain Arruda-Boyce). In this study, owing to its excellent performance in fitting uniaxial experimental data, a third-order Ogden model is adopted for the nonlinear hyperelastic spring. It has a strain-energy function as follows:

$$W = \sum_{i=1}^3 \frac{\mu_i}{\alpha_i} (\lambda_1^{\alpha_i} + \lambda_2^{\alpha_i} + \lambda_3^{\alpha_i} - 3) \tag{4}$$

In the above,  $\mu_i$  and  $\alpha_i$  ( $i = 1, 2, 3$ ) are the parameters of the model;  $\lambda = \frac{u}{L_i} + 1$  is the stretch of the material;  $u$  is the vertical deformation of the device; and  $L_i$  is the initial height or length of the rubber (depending on whether it corresponds to compression or tensile rubber, respectively).

From Eq. (4), the stress-stretch relation can be obtained (more details in “Appendix A: Hyperelasticity theory for rubber”) as follows:

$$P_{11}(\lambda) = \sum_{i=1}^3 \mu_i \left( \lambda^{\alpha_i-1} - \lambda^{-\left(\frac{\alpha_i}{2}+1\right)} \right) \tag{5}$$

Here,  $P_{11}$  is the uniaxial stress. Next, by substituting Eq. (5) into Eq. (3), the hyperelastic force-deformation relation can be obtained, as follows:

$$f_{hyp} = f(u)C_1 = P_{11}(\lambda)A_iC_1 \tag{6}$$

In Eq. (6),  $A_i$  is the initial cross-sectional area.  $C_1$  is a value such that  $f_{hyp}$  passes through the middle of the hysteretic cycles obtained in phase 2 (see Fig. 4). Usually,  $C_1$  should take a value between 0.5 and 0.8.

The six parameters of the third-order Ogden model must be chosen in such a way that Eq. (5) matches the softened loading curve of the tests. To obtain the parameters, a research curve fitting software for hyperelastic models called Hyperfit [57] was used. This software was developed under a MATLAB environment, and finds optimized constants for a given model in a non-linear least square sense, with the possibility of choosing different optimization algorithms. In this case, the Levenberg-Marquardt (L-M) optimization algorithm was used. The

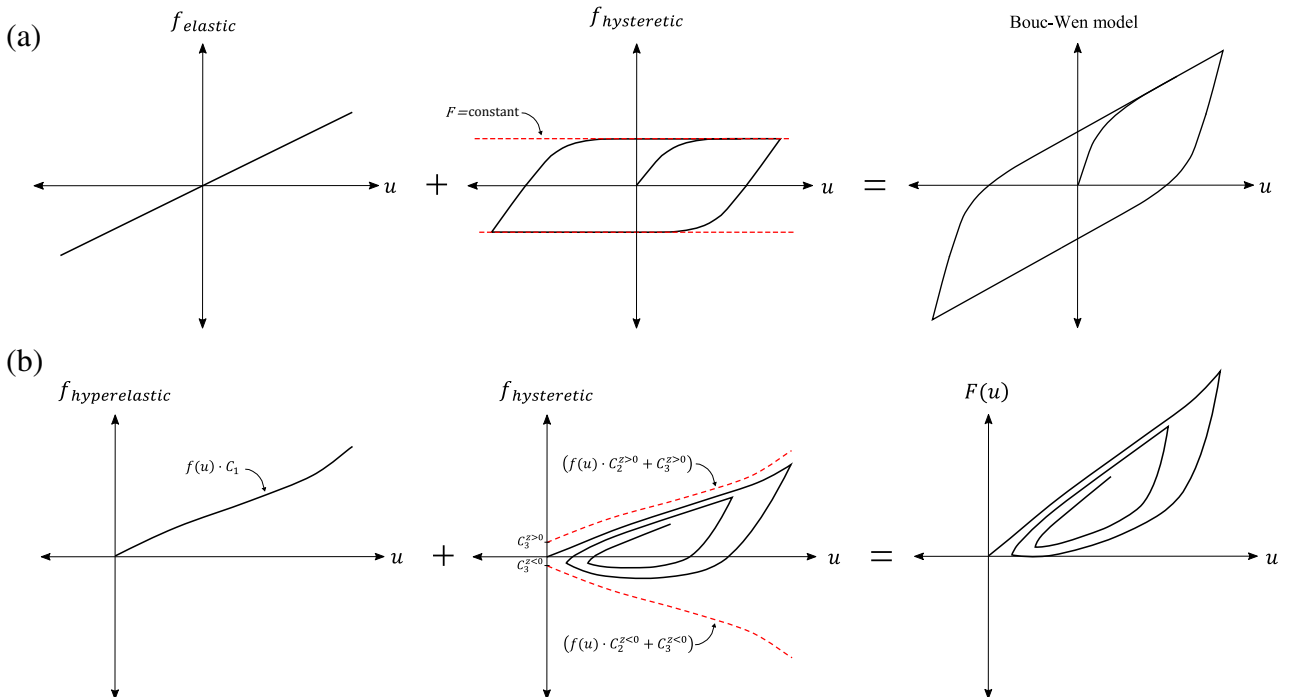


Fig. 8. (a) Classical Bouc-Wen model, (b) Hyperelastic Bouc-Wen model.

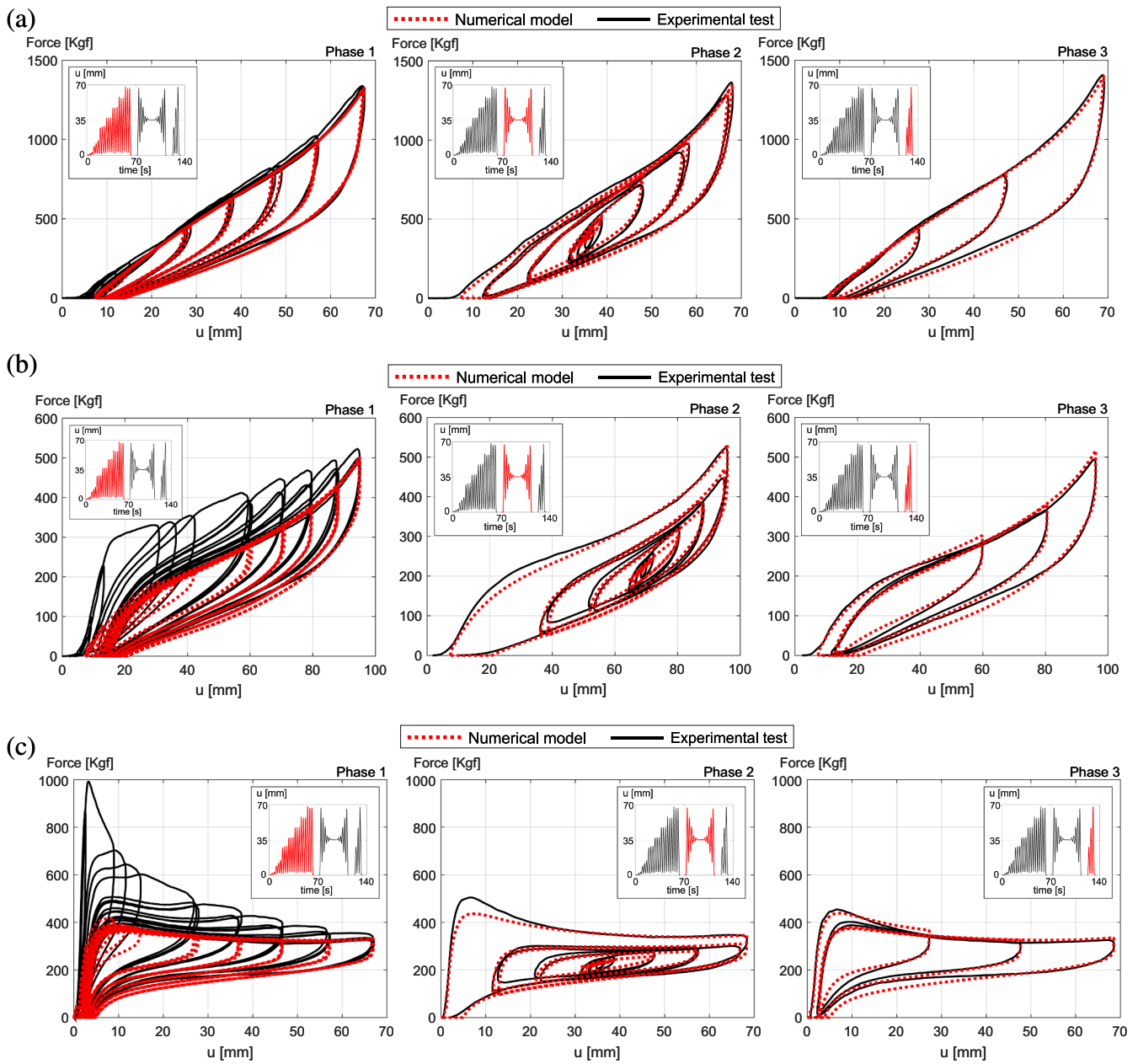


Fig. 9. Model fitting to experimental results of (a) compression rubber, (b) tensile rubber reversing the amplified kinematic of the framework (local uniaxial deformation), and (c) tensile rubber re-applying the kinematic amplification.

Table 4  
Relative error from model fitting.

	Compression Rubber	Tensile Rubber
All Phases	1.98%	13.02%
Phase 1	1.97%	17.84%
Phase 2	1.88%	4.47%
Phase 3	1.85%	4.75%

Table 5  
Identified parameters for the hyperelastic component.

	$\alpha_1$	$\alpha_2$	$\alpha_3$	$\mu_1$	$\mu_2$	$\mu_3$	$C_1$
Tensile	30.15	-5.68	1.94	4.5e-8	-16.73	-23.47	0.7
Compression	-4.97	-2.63	4.75	0.30	-15.17	-18.52	0.58

optimized parameters of the model for the tensile and compression behavior of the rubber are presented in Table 5.

Fig. 10 presents the fitting of the Ogden model to the softened loading curve obtained from the experimental tests for the stress-stretch relation of the compression and tensile rubber. The stress-stretch relation was obtained by dividing the force obtained in the tests by the initial cross-sectional area. In the case of the tensile rubbers, the data was modified according to the kinematic relation of the device to obtain the uniaxial behavior of the rubber. Although the solutions of the optimization that are local minimums are adequate for defining these parameters (as long as it is observed that the model fits the loading curve well), the third-order Ogden model might have difficulty converging for complex curves (owing to the large number of parameters). In such cases, any other hyperelastic model with fewer parameters can be used [58]; however, not all of them will fit the data in the same way.

No goodness-of-fit estimator used to analyze the optimization; although many adjustments could lead to local minima, for the purposes

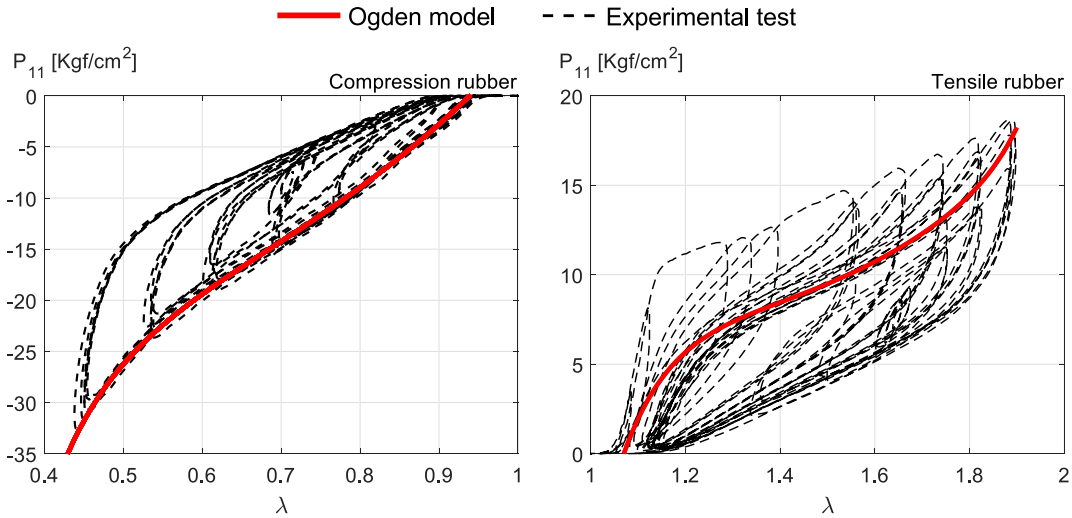


Fig. 10. Fitting of Ogden model to the softened loading curves of compression and tensile rubber.

of this work, a visual appreciation is sufficient for validating the results of the optimization. The fitting presented in Fig. 10 corresponds to the first local minima found by the L-M algorithm. It is important to mention that the Ogden model is a phenomenological model without a physical basis, so the validity range of the model is within the range of deformations where the parameters were calibrated (between 0.4 and 1.9). In fact, for values beyond the calibration range, it is highly probable that these models will diverge to unreasonable values.

#### 4.2. Hysteretic component

To obtain the hysteretic component, it is necessary to subtract the hyperelastic component  $f_{hyp} = f(u)C_1$  from the experimental data. The shape of this component should look like the idealized plot of  $f_{hys}$ , as shown in Fig. 8b.

The evolution in time of  $Z$  (Eq. (3)) is modeled using the same differential equation of the BW model [59] as follows:

$$\dot{Z} = \frac{1}{Y}A[1 - \{\beta \text{sign}(u\dot{Z}) + \gamma\}|Z|^n]\dot{u} \quad (7)$$

In the above  $A$ ,  $n$ ,  $\beta$ , and  $\gamma$  are parameters for controlling the hysteretic shape, and  $Y$  is the yield deformation of the model. In a typical formulation of the BW model,  $Z$  takes a value between 1 and  $-1$  (i.e.,  $A = 1$ ,  $\gamma + \beta = 1$ ), and  $Y$  is considered as a constant value, to set the pre-yield linear elastic stiffness when modeling the plasticity [59]. However, in the HBW model, the yield deformation  $Y$  is selected based on the direction of deformation (e.g., the value of  $\text{sign}(\dot{u})$ ) and the internal variable  $Z$ . With this approach, it is possible to generate four different branches in the hysterical cycle: loading, unloading, reloading in the opposite direction, and unloading again (See Fig. 11a). To create

a gradual change in the slope between unloading and reloading, the transition between different yield deformation values ( $Y$ ) is made through a hyperbolic tangent (See Fig. 11). Eq. (8) defines the value of  $Y$  as a function of the direction of deformation.

$$Y = \begin{cases} \tanh(C_4 \cdot Z) \frac{Y_1 - Y_2}{2} + \frac{Y_1 + Y_2}{2}, & \dot{u} \leq 0 \\ \tanh(C_5 \cdot Z) \frac{Y_3 - Y_4}{2} + \frac{Y_3 + Y_4}{2}, & \dot{u} > 0 \end{cases} \quad (8)$$

Here,  $C_4$  and  $C_5$  are constant values that control how quickly or smoothly the value of  $Y$  changes, and  $Y_i$  ( $i = 1, 2, 3, 4$ ) are the boundary values that  $Y$  can take. As the  $\tanh(x)$  function can only take values between 1 and  $-1$ , for the case  $\dot{u} \leq 0$ , if  $\tanh(C_4 \cdot Z) = 1$ , then  $Y = Y_1$ , whereas if  $\tanh(C_4 \cdot Z) = -1$ , then  $Y = Y_2$ . The same happens for the case  $\dot{u} > 0$  with the values  $Y_3$  and  $Y_4$ .

To simplify the calibration process, the parameters associated with the classic BW model are set as follows:  $A = 1$ ,  $n = 1$ ,  $\beta = 1$ , and  $\gamma = 0$ . These values cause the  $Z$  variable to increase gradually and slowly, i.e., consistent with the observed behavior of most rubber-like materials.

Parameters  $Y_1, Y_2, Y_3, Y_4, C_4$ , and  $C_5$  modify the yield deformation  $Y$  of the model, according to Eq. (8). The value of  $Y$  controls the speed at which the variable  $Z$  changes, and is reflected in the model as a slope. Fig. 11a schematically illustrates how the choice of different  $Y$  values changes the slope of the model, according to the branches considered in Eq. (8). A larger value of  $Y$  generates a small slope suitable for the branches associated with  $Y_2$  and  $Y_3$ , whereas a small value of  $Y$  generates a large slope suitable for the branches associated with  $Y_1$  and  $Y_4$ . The use of a hyperbolic tangent for the transition between two values of  $Y$  provides a smooth change of the curve, avoiding undesired corners in the model, as shown in Fig. 11a.

Parameters  $C_4$  and  $C_5$  (inside the hyperbolic tangent argument)

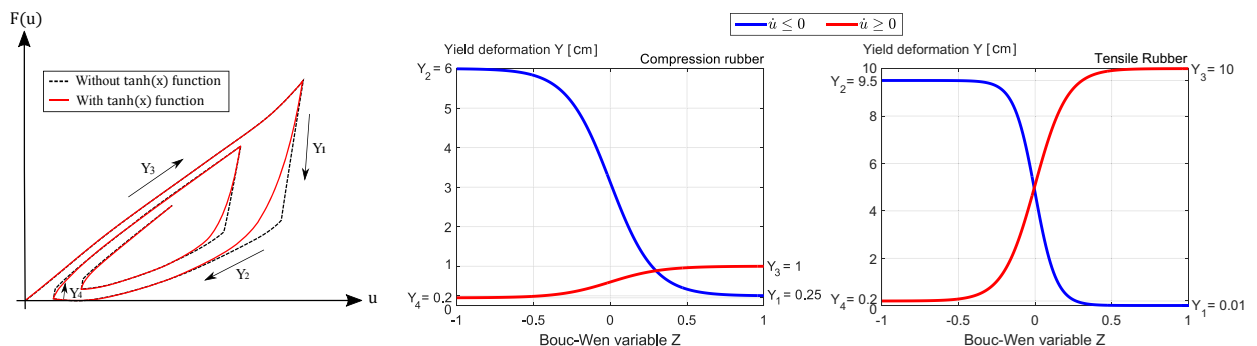


Fig. 11. Variable yield deformation of the Hyperelastic Bouc-Wen model.

control the speed at which the transition occurs. High values of these parameters will result in a fast transition, whereas small values will result in a slow transition. It is important to mention that if the values of these parameters are too small, the transition will not occur entirely within the range of the variable  $Z$  (between  $-1$  and  $1$ ). As an example, in Fig. 11b, it is observed that for the compression rubber, the transition occurs almost entirely between the values of  $Z = [-0.5, 0.5]$ . In contrast, for tensile rubber where the values of these parameters result in higher values in the calibration, the transition occurs mostly between the values of  $Z = [-0.25, 0.25]$  (approximately).

Finally, the last four parameters ( $C_2^{Z<0}$ ,  $C_2^{Z>0}$ ,  $C_3^{Z<0}$ , and  $C_3^{Z>0}$ ) define the boundaries of the model that multiply the variable  $Z$ . In the classical formulation of the BW model, the boundaries correspond to a constant force that is independent of the level of deformation. In the HBW, the limits are given by the same hyperelastic component of the model  $f(u)$  which varies with the level of deformation; however, it is also weighted by  $C_2$ , and summed to  $C_3$ . Fig. 8b shows the shape that these limits take. As the model is intended to represent the compression or tensile behavior of the rubber, there is only positive deformation (i.e.,  $u > 0$ ). Parameter  $C_2$  controls the slope of the boundary curve  $f(u)$ , allowing the hysteresis to be lifted to different degrees for small and large deformations. In contrast, parameter  $C_3$  controls the position in the  $Y$ -axis of the boundary, allowing the hysteresis to be lifted uniformly.

The identified parameters for the model are listed in Table 6. It is important to mention that this calibration was performed completely manually, without the use of any optimization algorithm.

## 5. Horizontal constitutive relations of the ISO3D-2G device

As all devices are simply supported, there is a frictional interaction between the device and the ground. Generally, the friction is modeled by a transition between a stick and a slip phase. This is usually considered with the respective transitional rules; in contrast, in this study, the non-linear biaxial hysteretic model proposed by Park et al. [60] is used. This model acts like a fictitious spring, with a given stiffness during the non-slip phase, and zero stiffness during the slip phase. The forces of the interaction in  $X$  and  $Y$  directions are given as follows:

$$\begin{pmatrix} F_x \\ F_y \end{pmatrix} = F_v(u, Z)\mu \begin{pmatrix} Z_x \\ Z_y \end{pmatrix} \quad (9)$$

In the above,  $F_v(u, Z)$  corresponds to the vertical axial load of the device as obtained from Eq. (3), and  $\mu$  is the friction coefficient between the surfaces in contact. Multiplying both provides the yield or sliding force of the frictional model. Commonly, the slide between the surfaces is caused by a high lateral force that exceeds the restitutive force  $F_v(u, Z)\mu$ . In the case of the VRI system, the sliding condition only happens in some devices, owing to a drastic reduction of the axial load  $F_v(u, Z)$  from the unloading in some legs during the rocking motion of the system. The choice of the friction coefficient must be made according to the contact surfaces. Considering the interaction between steel and concrete, some authors have experimentally determined that a suitable friction coefficient during sliding for high axial loads is between 0.5 and 0.7 [61,62]. However, as sliding is also expected to occur

for low axial loads, a friction coefficient of 0.3 is adopted for the model [63].

The hysteretic components of the model  $Z_x$  and  $Z_y$  are the solution of the coupled differential equation as follows:

$$\begin{aligned} & \frac{F_v(u, Z)\mu}{K_f} \begin{pmatrix} \dot{Z}_x \\ \dot{Z}_y \end{pmatrix} \\ & = \begin{bmatrix} A - \beta \text{sgn}(Z_x \dot{u}_x) Z_x^2 - \gamma Z_x^2 & -\beta \text{sgn}(Z_y \dot{u}_y) Z_x Z_y - \gamma Z_x Z_y \\ -\beta \text{sgn}(Z_x \dot{u}_x) Z_x Z_y - \gamma Z_x Z_y & A - \beta \text{sgn}(Z_y \dot{u}_y) Z_y^2 - \gamma Z_y^2 \end{bmatrix} \begin{pmatrix} \dot{u}_x \\ \dot{u}_y \end{pmatrix} \end{aligned} \quad (10)$$

Here,  $A = 1$ ,  $\beta = 0.5$ , and  $\gamma = 0.5$  are the parameters of the biaxial BW model,  $\dot{u}_x$  and  $\dot{u}_y$  are the velocities in  $X$  and  $Y$  direction, respectively, and the term  $F_v(u, Z)\mu/K_f$  is the yield deformation of the model. This yield deformation constantly varies with the axial load, to maintain a constant stiffness  $K_f$  at the non-slip phase. Generally, this lateral stiffness is considered at a very high value to obtain a small yield deformation and therefore a small non-slip phase, as consistent with the friction theory. However, the presence of various elements between the structure and the ground provides enough flexibility to consider the appropriate use of an equivalent lateral stiffness  $K_{eq}$  instead for the non-slip phase.

The equivalent lateral stiffness considered in the analysis is chosen according to the structure geometry and materials. For most industrial equipment, this stiffness is high, and its flexibility can be neglected in the analysis. In the case of some flexible structures (e.g., a legged steel wine storage tank where the link between the device and the rest of the structure is the leg of the tank), additional flexibility should be considered. Thus, the equivalent lateral stiffness  $K_{eq} = K_f$  for the non-slip phase of the frictional model can be estimated as two springs connected serially, as follows:

$$K_{eq}(u) = \left( \frac{1}{K_{device}(u)} + \frac{1}{K_{structure}} \right)^{-1} \quad (11)$$

$K_{device}(u)$  is the lateral stiffness of the device as estimated from Eq. (12), and  $K_{structure}$  is the lateral stiffness of the element connecting the device to the main body of the isolated structure. Fig. 12 represents the case for a legged wine storage tank, where the leg of the tank is considered as a flexible element.

The lateral stiffness of each device incorporates the stiffness of the central rod, flexible element, and support structure. All these stiffnesses remain constant except for that of the central rod, which changes its flexural length according to the vertical deformation  $u$  of the device. The stiffness of the device can be estimated as follows:

$$K_{device}(u) = \left( \frac{1}{K_{rod}(u)} + \frac{1}{K_{flex}} + \frac{1}{K_{supp}} \right)^{-1} \quad (12)$$

The articulated framework structure is designed to not contribute to lateral stiffness; as such, a sufficiently large gap in the articulated connections must be considered to allow this. If the stiffness of the flexible element  $k_{flex}$  is very low as compared to that of the other two components, this stiffness will predominate, and the stiffness of the entire device will be nearly-independent of the vertical deformation  $u$  (i.e.,  $\frac{\partial K_{device}(u)}{\partial u} \approx 0$ ). In fact, if the bushing is much more flexible than the

**Table 6**  
Identified parameters for the hysteretic component.

	Bouc-Wen				Yield deformation $Y$ [cm]				Bounds curves of Bouc-Wen					
	$\beta$	$\gamma$	$n$	$A$	$Y_1$	$Y_2$	$Y_3$	$Y_4$	$C_4$	$C_5$	$C_2^{Z>0}$	$C_3^{Z>0}$	$C_2^{Z<0}$	$C_3^{Z<0}$
Tensile	1	0	1	1	0.01	9.5	10	0.2	7.3	4.75	0.3	4.5	0.47	4.5
Compression	1	0	1	1	0.25	6	1	0.2	3.5	3	0.36	40	0.35	100

\*  $C_3^{Z>0}$  and  $C_3^{Z<0}$  are in [kgf] units.

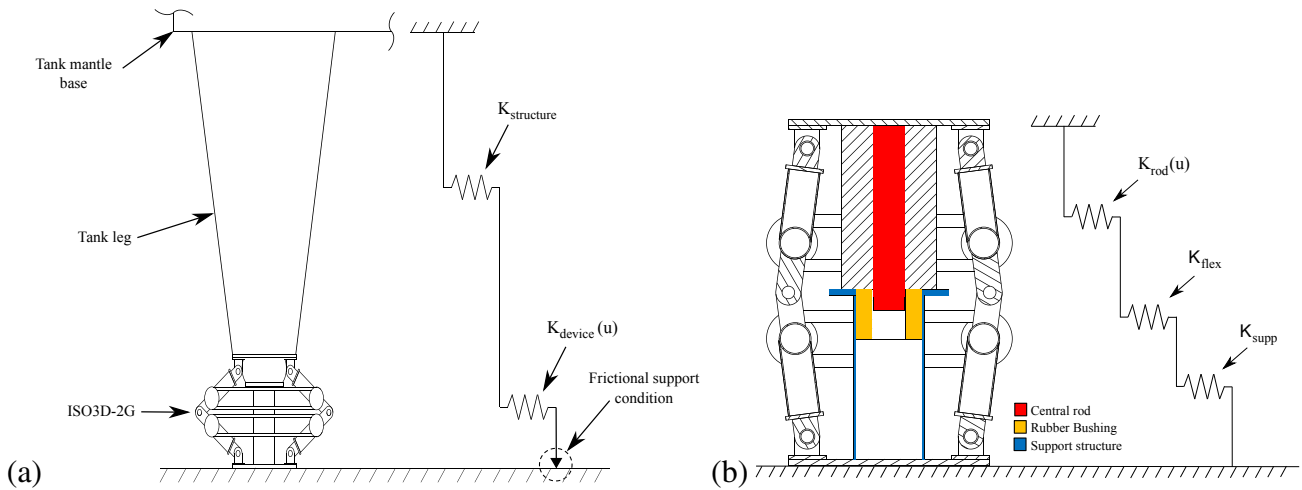


Fig. 12. (a) Simplified model for the equivalent lateral stiffness of the connection to the device, (b) Idealized model for the lateral stiffness of the device.

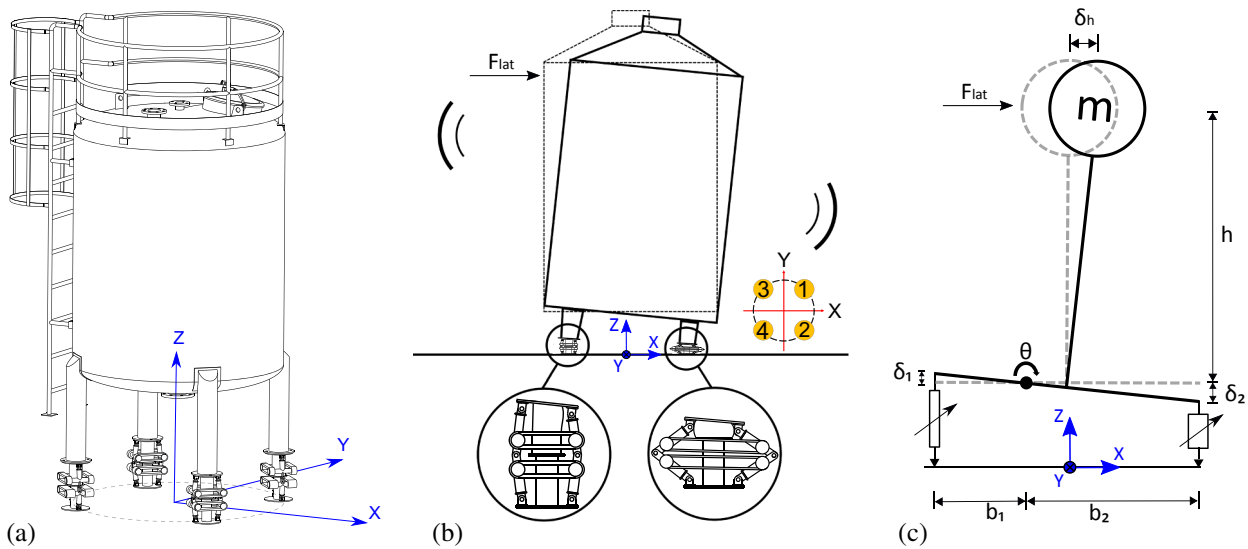


Fig. 13. (a) Three-dimensional view of an isolated storage tank, (b) bi-dimensional rocking motion with the numeration of the devices, and (c) idealized lumped-mass model.

other two elements, the lateral stiffness can be assumed as equal to the radial stiffness of the bushing, i.e.,  $K_{device} = K_{flex}$ .

The estimation of the radial stiffness of a rubber bushing is a widely studied subject in the literature [64–68], varying between approximately 1–2 Tonf/cm for a high-damping rubber bushing when considering a shear modulus for the rubber between 0.6 and 1.3 MPa [66]. This estimation was computed for a bushing size suitable for a device with the dimensions presented in Table 2, while maintaining the scale and aspect ratio shown in Fig. 12b. As a conservative approach, a stiffness value of  $K_{flex} = 2\text{Tonf/cm}$  was considered in this work for the flexible element. The authors believe that a rubber bushing is the best option for use as a flexible element in the ISO3D-2G device, as it allows the rotation of the rod, and the properties can be considered as rate-independent for the range of frequencies in seismically isolated structures [69].

The lateral stiffness of the support structure and central rod can be estimated as a cantilever frame element with their corresponding properties. However, in the case of the rod, its length is continuously changing owing to the vertical deformation  $u$ , as follows:

$$K_{rod}(u) = \frac{3E_r I_r}{(L_r - u)^3} \quad (13)$$

Here  $E_r$ ,  $I_r$ , and  $L_r$  are the Young's modulus, moment of inertia, and

length of the rod, respectively. As a result of all these considerations, the ISO3D-2G device is vertically flexible in the U-direction, and is laterally stiff in any radial R-direction (the directions refer to Fig. 1a). Thus, it is able to distribute lateral forces in all devices, unlike the ISO3D device, which only had some devices acting simultaneously in a stiff direction (a detailed explanation of why the ISO3D only has one stiff direction can be found in references [24,30]).

Based on all of these considerations, the estimated lateral stiffness of the devices, as computed with Eq. (12), is  $K_{device} = 1.6\text{Tonf/cm}$ . It can be seen that this value is very close to the value considered for the flexible element.

## 6. Case STUDY: ISO3D-2G device performance

In this section, the dynamic behavior of the proposed isolation system is analyzed through a time-history analysis. Owing to the unsatisfactory performance of legged wine storage tanks in strong seismic events worldwide [26–29], these structures are particularly attractive for applying the proposed VRI system, as materialized with the ISO3D-2G device. This system is characterized by three low-frequency modes: vertical translation, and rotation around two horizontal axes; and three high-frequency modes: translation in two horizontal axes, and rotation around the vertical axis. A schematic rendered animation video of a

**Table 7**  
Geometric properties of the tank and separation of devices.

Tank mantle radius (cm)	Separation of devices in x-dir $b_1 + b_2$ (cm)	Separation of devices in y-dir $b_1 + b_2$ (cm)	Mantle height (cm)	$h$ Center of mass height (cm)	x-dir aspect ratio $\left(\frac{b_1 + b_2}{2h}\right)$	y-dir aspect ratio $\left(\frac{b_1 + b_2}{2h}\right)$
80	100	106	158.5	168.3	0.297	0.315

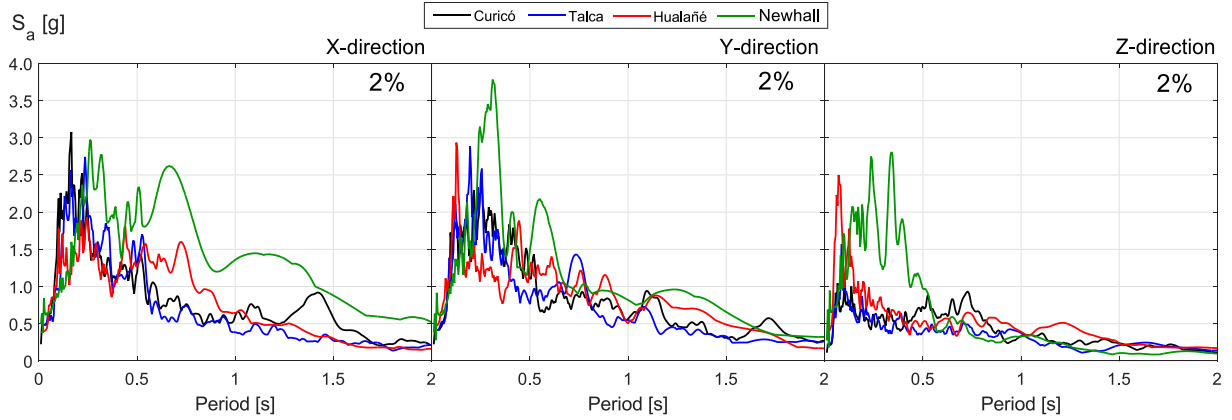


**Fig. 14.** Pseudo-acceleration spectra for 2% of damping ratio.

wine storage tank protected with the VRI system, as well as the ISO3D-2G device, can be found in Ref. [70].

Fig. 13 presents an isometric view of an isolated storage tank with four ISO3D-2G devices, a schematic bi-dimensional rocking motion, and an idealized model considered suitable for the VRI system. This model consists of a six degrees-of-freedom rigid structure, with a mass  $m$  concentrated at a height  $h$  above the mass-less isolation level. Auad and Almazán [30] showed that the difference between using a complete fluid-structure interaction model and a quasi-static approach for liquids in a storage tank full of wine is truly negligible. This assumption is in line with practice, as for winemaking purposes, these tanks must remain fully filled. As such, a rigid body with equivalent inertial properties is used to represent the storage tank with liquid. These properties are defined according to the liquid sloshing dynamics theory [71,72].

The tank under consideration is the same one used by Colombo & Almazán [73]. The weight of the tank is approximately 3200 kgf (including the liquid inside), and has four legs, each 89 cm in height. The geometric properties are listed in Table 7.

### 6.1. Equation of motions

The equation for the motion of the structure, assuming linear kinematics, can be expressed as follows:

$$\mathbf{M}\ddot{\mathbf{q}}(t) + \mathbf{K}_{geo}\mathbf{q}(t) + \mathbf{L}^T\mathbf{F}_{NL}(t) = \mathbf{W} - \mathbf{S}\ddot{\mathbf{u}}_g(t) \quad (14)$$

$$\mathbf{M} = \begin{bmatrix} m & 0 & 0 & 0 & mh & 0 \\ 0 & m & 0 & -mh & 0 & 0 \\ 0 & 0 & m & 0 & 0 & 0 \\ 0 & -mh & 0 & (mh^2 + I_y) & 0 & 0 \\ mh & 0 & 0 & 0 & (mh^2 + I_x) & 0 \\ 0 & 0 & 0 & 0 & 0 & I_z \end{bmatrix}$$

$$\mathbf{K}_{geo} = \begin{bmatrix} 0 & 0 & 0 & 0 & 0 & 0 \\ 0 & 0 & 0 & 0 & 0 & 0 \\ 0 & 0 & 0 & 0 & 0 & 0 \\ 0 & 0 & 0 & -mh(g + \ddot{u}_{gz}(t)) & 0 & 0 \\ 0 & 0 & 0 & 0 & -mh(g + \ddot{u}_{gz}(t)) & 0 \\ 0 & 0 & 0 & 0 & 0 & 0 \end{bmatrix}$$

$$\mathbf{S} = \begin{bmatrix} m & 0 & 0 \\ 0 & m & 0 \\ 0 & 0 & m \\ 0 & -mh & 0 \\ -mh & 0 & 0 \\ 0 & 0 & 0 \end{bmatrix}$$

$$\mathbf{W} = [0 \ 0 \ -mg \ 0 \ 0 \ 0]^T$$

$$\mathbf{q}(t) = [u_x(t) \ u_y(t) \ u_z(t) \ \theta_y(t) \ \theta_x(t) \ \theta_z(t)]^T$$

$$\ddot{\mathbf{u}}_g(t) = [\ddot{u}_{gx}(t) \ \ddot{u}_{gy}(t) \ \ddot{u}_{gz}(t)]^T$$

In the above,  $\mathbf{q}(t)$  is the vector of the degrees of freedom;  $\mathbf{M}$  and  $\mathbf{K}_{geo}$  are the mass and geometric stiffness matrices, respectively;  $\mathbf{W}$  the self-weight vector;  $g$  is the gravity acceleration;  $m$  is the equivalent lumped mass of the system;  $h$  is the height of the lumped mass,  $I_x$ ,  $I_y$ ,  $I_z$  are the equivalent rotational inertia of the lumped mass around the principal axes;  $\mathbf{F}_{NL}(t)$  is a vector of the local non-linear forces of the devices, with  $\mathbf{L}$  as a kinematic transformation matrix;  $\ddot{\mathbf{u}}_g(t)$  is the ground acceleration vector; and  $\mathbf{S}$  the load matrix. The geometric stiffness matrix involves P-delta effects, owing to the constant gravity acceleration  $g$  and the additional vertical acceleration of the ground.

### 6.2. Seismic records

To analyze the performance of the isolation system, the model was subjected to four records: a Newhall record from the 1994  $M_w$  6.7 Northridge Earthquake, and three other records (Curicó, Hualañé, and Talca) from the 2010  $M_w$  8.8 Maule Earthquake. The reason for considering the Northridge Earthquake is that in these types of motions (impulsive-like), the system is expected to have a large lateral displacement, which would consequently cause an uplifting of the system.

Fig. 14a shows the computed pseudo-acceleration response spectra for the three components of the records for 2% of equivalent viscous damping (a widely accepted damping for anchored steel storage tanks) [74,75]. The considered tank has a fixed base period of approximately 0.3 s [30]; thus, spectral accelerations of up to 2 g would be expected for the Maule earthquake, and up to 3.5 g for the Northridge earthquake.

In seismically isolated structures, the flexibilization effect leads to larger lateral displacements during a seismic event. The displacements

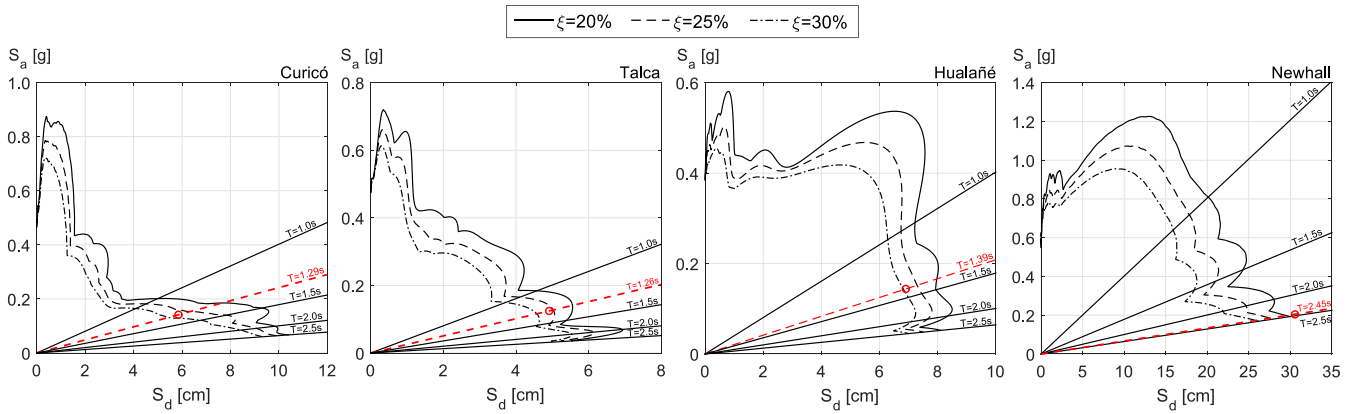


Fig. 15. Pseudo-displacement vs Pseudo-acceleration spectrum in X-direction for 20%, 25%, and 30% of damping ratio.

of a structure isolated with a VRI system are also larger than those of the same structure with a fixed base. This is an important consideration for the desired performance, as these structures are usually inside industrial facilities where there is a high probability of impact with other nearby elements such as beams, gangways, other tanks, and connection piping. To estimate the expected lateral displacement and acceleration of the system, the  $S_a - S_d$  spectra were computed for the X components of the records for 20%, 25%, and 30% of damping. Fig. 15 presents these spectra, specifying the periods 1.0, 1.5, 2.0, and 2.5, and the period identified for the system in Subsection 6.3 for each record.

6.3. Results

This subsection presents the results obtained from the time-history analysis of the four seismic records. For comparison purposes, results were obtained considering both the three components of the records (3D-THA), and only the component of higher intensity (1D-THA) applied in the X direction.

Fig. 16 presents the relation between the horizontal displacement of the center of mass (CM) and the base shear of the structure for the 1D-THA system. Its effective stiffness and damping ratio are also identified. For the three records corresponding to the Maule Earthquake, the

observed behavior is similar to that of conventional isolation systems. The effective period varies between 1.26 s and 1.39 s, and the effective damping ratio varies between 0.26 and 0.29. The maximum values of the base shear and CM displacement are consistent with those shown in Fig. 15. However, for the Newhall record, there is a significant change in the pattern of behavior, owing to the uplift of two of the four devices. In this case, the uplift occurs at a CM displacement of approximately 11 cm.

It can be seen that after the uplifting, as the displacement increases, the base shear decreases. This reduction in the base shear is because the CM of the structure approaches a point where it is pivoting, reducing the restitutive force that provides the self-weight of the system. The latter is consistent with the results obtained in other research regarding rocking with large uplifting [76–80].

Table 8 presents the maximum global response values of the structure: the total base shear, dynamic vertical reaction (subtracting the static component  $W$ ), and total horizontal displacement. The ratio between the values obtained for 3D-THA and 1D-THA is also indicated. For the 1D-THA system, a component of higher intensity was applied in the X direction of the model. According to the ratios, it can be seen that the 1D-THA system is appropriate for estimating the total horizontal displacement, but not for estimating the global forces, especially the dynamic vertical reaction. To quantify the effects of isolation in both

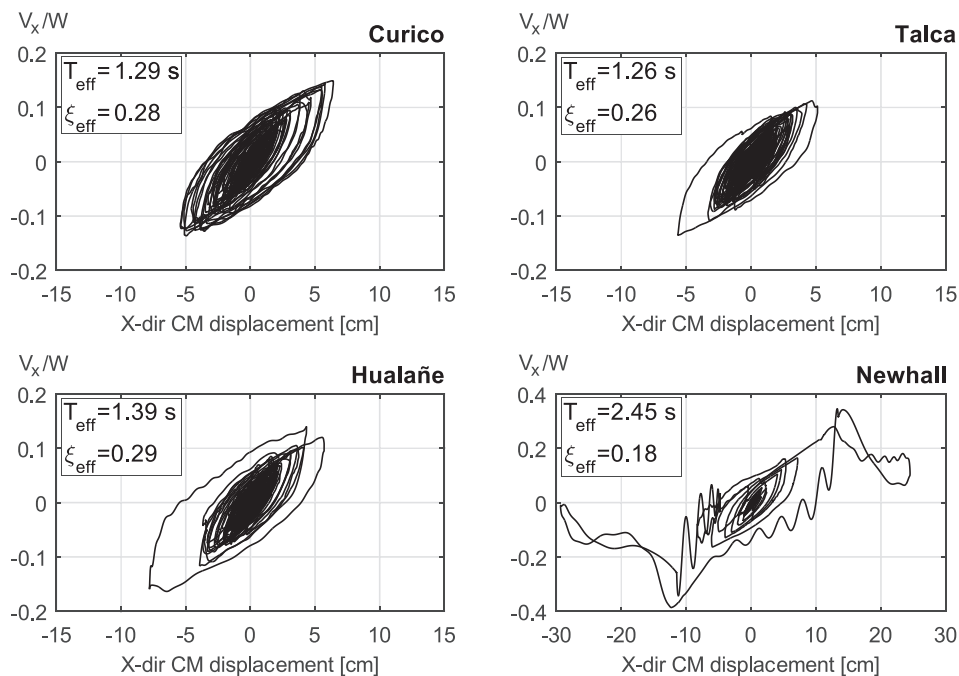


Fig. 16. Base shear vs. center of mass lateral displacement relationship for the four considered records.

**Table 8**  
Global results for the system.

Record	1D-THA			3D-THA*			Ratio 3D/1D			Ratio fixed Base/isolated base (FB/IB)	
	$\frac{V_T^{max}}{W}$	$\frac{\Delta P_Z^{max}}{W}$	$u_T^{max}$ [mm]	$\frac{V_T^{max}}{W}$	$\frac{\Delta P_Z^{max}}{W}$	$u_T^{max}$ [mm]	V	$\Delta P_Z$	$u_T$	V	$\Delta P_Z$
Curicó-y	0.176	0.14	77.8	0.23	0.29	78.7	1.31	2.07	1.01	7.92	1.99
Talca-x	0.136	0.10	56.5	0.18	0.22	64.8	1.32	2.20	1.14	10.94	3.45
Hualañé-y	0.200	0.11	84.2	0.20	0.42	81.8	1.00	3.82	0.97	7.41	3.78
Newhall-x	0.387	0.74	293.6	0.55	1.05	274.3	1.42	1.42	0.93	6.63	0.70
						Mean	1.26	2.37	1.01	8.22	2.48

\* Total base shear is computed as  $V_T^{max} = \max(\sqrt{V_x(t)^2 + V_y(t)^2})$ , where  $t$  is each time instant of the analysis. Total displacement is computed in the same way.

directions, the ratios between the maximum force values obtained for a fixed base and isolated base condition (reduction factor) are presented. It can be seen that the average reduction factor in the horizontal direction is 8.44, i.e., in the same order as that the conventional lateral isolation systems, whereas the average reduction factor in the vertical direction is 2.48.

Table 9 presents the maximum local response values for each device (numbered according to Fig. 13b): the total base shear, vertical reaction, and total horizontal displacement. It can be seen that to estimate the local responses, it is necessary to consider the three components of ground motion. Notably, for the three non-impulsive records, there is no uplift on any of the four devices.

## 7. Conclusions

In this work, the effectiveness of a VRI system was analyzed. To materialize the isolation system, an improved version of the ISO3D device, called ISO3D-2G, was developed. The most significant changes made were the addition of a solid central rod, and the replacement of all steel springs with high-damping rubber bearings.

Three prototypes of the ISO3D-2G were tested with different rubber configurations, to analyze the contributions of rubber bearings in

compression and tension independently. A three-phase load protocol was applied, as specially designed for this type of device. Each phase had the purpose of showing a specific behavior of the rubbers.

After all phases of the test, the effective stiffness remained approximately constant, varying between 22.1 kgf/mm and 25.5 kgf/mm, whereas the effective damping ratio tended to decrease with the deformation amplitude, varying between 15.7% and 25.7%. In all phases, the dissipated energy increased with the deformation amplitude, with a power close to 3/2.

Based on the experimental results, a novel model (the HBW) was developed to represent the vertical force-deformation relation of the rubber bearings under uniaxial deformation. The HBW model was composed of a modified BW model for highly asymmetric hysteresis, connected in parallel to a nonlinear hyperelastic spring. The model was manually calibrated to minimize the error in the dissipated energy, reaching relative errors of less than 2% and 5% for the compression and tensile rubber bearings, respectively. The model was very accurate for different displacement patterns and levels of deformation. This allows for the possibility of representing the complex hysterical behaviors of elastomers under compression and tension for other applications. The lateral behavior of the device was represented using a non-linear 2D frictional hysteretic model. No important sliding was observed in the

**Table 9**  
Local results for each device

Record	1D-THA				3D-THA					Ratio 3D/1D			
	$\frac{v_{device}^{max}}{W/4}$	$\frac{p_{device}^{max}}{W/4}$	$u_{max}$ [mm]	$u_{min}$ [mm]	Leg	$\frac{v_{device}^{max}}{W/4}$	$\frac{p_{device}^{max}}{W/4}$	$u_{max}$ [mm]	$u_{min}$ [mm]	V	P	$u_{max}$	$u_{min}$
Curicó	0.308	1.712	54.1	8.3	1	0.28	2.20	63.5	1.7	0.91	1.29	1.17	0.20
	–	–	–	–	2	0.42	2.56	65.6	6.0	1.04	1.50	1.21	0.72
	–	–	–	–	3	0.24	2.36	63.6	1.4	0.78	1.38	1.18	0.17
	–	–	–	–	4	0.40	2.56	65.5	2.9	1.30	1.50	1.21	0.35
				Mean		0.32	2.44	64.6	3	1.00	1.42	1.19	0.36
Talca	0.196	1.596	52.9	18.0	1	0.24	2.08	60.5	10.3	1.22	1.30	1.14	0.57
	–	–	–	–	2	0.20	1.84	56.3	9.2	1.02	1.15	1.06	0.51
	–	–	–	–	3	0.16	2.12	61.0	19.2	0.82	1.33	1.15	1.07
	–	–	–	–	4	0.24	2.24	62.4	5.1	1.22	1.40	1.18	0.28
				Mean		0.20	2.08	60.1	11.0	1.07	1.30	1.13	0.61
Hualañé	0.364	1.852	54.9	5.5	1	0.20	1.80	56.9	3.7	0.55	0.97	1.04	0.67
	–	–	–	–	2	0.24	2.12	60.5	–8.4	0.66	1.14	1.10	–
	–	–	–	–	3	0.28	2.44	67.4	6.7	0.77	1.32	1.23	1.22
	–	–	–	–	4	0.20	0.51	59.9	13.9	0.55	1.10	1.09	2.53
				Mean		0.24	2.04	61.18	3.98	0.63	1.13	1.12	1.47
Newhall	0.776	2.98	70.7	–117.4	1	0.84	4.12	76.0	–110.5	1.08	1.38	1.07	0.94
	–	–	–	–	2	1.20	5.28	77.7	–121.7	1.55	1.77	1.10	1.04
	–	–	–	–	3	1.36	7.00	81.0	–80.0	1.75	2.35	1.15	0.68
	–	–	–	–	4	1.00	5.24	77.2	–89.9	1.29	1.76	1.09	0.77
				Mean		1.12	5.40	77.98	–100.53	1.42	1.82	1.10	0.86
								Mean	1.0	1.42	1.14	0.8	

devices during the time history analyses.

To analyze the performance of the isolation system, an idealized model with six degrees of freedom was considered. The model was subjected to three subduction type records (non-impulsive) and one cortical-type record (impulsive). For the three non-impulsive records, the observed behavior was similar to that of conventional lateral isolation systems. Horizontal force reduction ratios between 7.4 and 10.9 were obtained. The maximum shear base remained below 23% of the total weight of the structure, even considering the three components of the ground motions. In contrast, vertical force reduction ratios between 2 and 3.8 were obtained, demonstrating that the vertical isolation effect is very satisfactory. For the impulsive record, there was a significant change in the pattern of behavior, owing to a large uplifting of approximately 120 mm on two of the four devices. Despite the above, the structure remained stable, and the lateral isolation effect was preserved.

Finally, it is concluded that the use of vertically flexible devices with high damping in the base of some structures to generate a rocking isolation mechanism is an effective way to reduce the seismic demand on the structure, even though the isolated modes of the structure do not take periods longer than 2.0 s. Although there is not a complete lateral translation at the base, the VRI system isolates the structure by allowing the lateral and vertical displacement of the CM.

## Appendix A. Hyperelasticity theory for rubber

If we consider that a given particle of material at a time  $t_0$  is located at a point  $\mathbf{P}_1 = [x_1, y_1, z_1]$ , and that after deformation of the material, the same particle at time  $t$  is located at the position  $\mathbf{P}_2(\mathbf{P}_1, t) = [x_2, y_2, z_2]$ , the local gradient of deformation is defined as follows:

$$\mathbf{F}(\mathbf{P}_1, t) = \frac{\partial \mathbf{P}_2(\mathbf{P}_1, t)}{\partial \mathbf{P}_1} \quad (\text{A.1})$$

If we consider an incompressible and isotropic uniaxial strain deformation, the principal stretches are related by  $\lambda_2 = \lambda_3 = \lambda_1^{-\frac{1}{2}}$ . Then, we have that  $x_2 = \lambda_1 x_1$ ,  $y_2 = \lambda_1^{-\frac{1}{2}} y_1$  and  $z_2 = \lambda_1^{-\frac{1}{2}} z_1$ ; the principal stretch in the 1-direction  $\lambda_1$  will be represented as  $\lambda$ . Using the left Cauchy-Green strain tensor  $\mathbf{B} = \mathbf{F}\mathbf{F}^T$  as the measure of deformation, we obtain the principal invariants  $I_1 = \text{tr}(\mathbf{B}) = \lambda^2 + 2\lambda^{-1}$ ,  $I_2 = \frac{1}{2}\{(\text{tr}\mathbf{B})^2 - \text{tr}(\mathbf{B}\mathbf{B})\} = \lambda^{-2} + 2\lambda$ , and  $I_3 = \det(\mathbf{B}) = 1$ .

To represent the internal forces on the material, two stress tensors are commonly used: (i) the true stress (Cauchy stress) tensor  $\sigma$ , and (ii) the engineering stress (first Piola-Kirchhoff stress) tensor  $\mathbf{P}$ . Both are related by  $\mathbf{P} = \det(\mathbf{F})\sigma\mathbf{F}^{-T}$ . According to the hyperelasticity theory, these stress tensors are derived from a strain-energy function  $W$ . This function depends on the strain tensor  $\mathbf{B}$ , specifically on the invariants in the case of an isotropic material, and only on  $\lambda$  in the case of uniaxial deformation. With all of these considerations, the relation between the engineering stress (first Piola-Kirchhoff stress) and the stretch can be expressed as follows [81]:

$$\mathbf{P} = \frac{\partial W(I_1(\lambda), I_2(\lambda))}{\partial \mathbf{F}} - p\mathbf{F}^{-T} \quad (\text{A.2})$$

Here,  $p$  is a parameter of arbitrary pressure. As the uniaxial behavior is of interest in this work, imposing the condition  $P_{22} = P_{33} = 0$  for  $p$  parameter leads to a uniaxial stress expression as follows:

$$P_{11}(\lambda) = \frac{\partial W(I_1(\lambda), I_2(\lambda))}{\partial \lambda} = 2(\lambda - \lambda^{-2}) \left( \frac{\partial W(I_1(\lambda), I_2(\lambda))}{\partial I_1(\lambda)} + \frac{1}{\lambda} \frac{\partial W(I_1(\lambda), I_2(\lambda))}{\partial I_2(\lambda)} \right) \quad (\text{A.3})$$

The same procedure can be used to obtain the stress-stretch relation for the equibiaxial extension, pure shear, and biaxial extension. These are the most common and standardized tests with simple loading conditions for characterizing a specific material. Many authors have proposed strain-energy functions to represent the behaviors of these types of materials.

As mentioned in Section 4, the third-order Ogden model is adopted for the nonlinear hyperelastic spring, and has a strain-energy function as follows:

$$W = \sum_{i=1}^3 \frac{\mu_i}{\alpha_i} (\lambda_1^{\alpha_i} + \lambda_2^{\alpha_i} + \lambda_3^{\alpha_i} - 3) \quad (\text{A.4})$$

Replacing this function in Eq. (A.3) we obtain the stress-stretch relation for the third-order Ogden model as follows:

$$P_{11}(\lambda) = \sum_{i=1}^3 \mu_i \left( \lambda^{\alpha_i-1} - \lambda^{-\left(\frac{\alpha_i}{2}+1\right)} \right) \quad (\text{A.5})$$

## Appendix B. Supplementary material

Supplementary data to this article can be found online at <https://doi.org/10.1016/j.engstruct.2020.110595>.

## CRedit authorship contribution statement

**Sergio I. Reyes:** Conceptualization, Methodology, Software, Validation, Investigation, Writing - original draft, Visualization, Funding acquisition. **José L. Almazán:** Conceptualization, Investigation, Resources, Writing - review & editing, Supervision, Project administration, Funding acquisition.

## Acknowledgment

The authors are grateful for the support granted by the project ANID/FONDEF/IT15110037, as well as ANID/FONDAP/15110017 "Research Center for Integrated Disaster Risk Management (CIGIDEN)", and ANID/FONDECYT/1170836 "SIBER-RISK: Simulation Based Earthquake Risk and Resilience of Interdependent Systems and Networks". Also, to Brain Chile entrepreneurship program and the Transfer and Development Department of the Pontificia Universidad Católica de Chile for the support provided in the patenting process of the presented technology. In addition, thank the help provided by the team of the laboratory of the Department of Structural and Geotechnical Engineering of the same university.

## References

- [1] Papazoglou AJ, Elnashai AS. Analytical and field evidence of the damaging effect of vertical earthquake ground motion. *Earthq Eng Struct Dyn* 1996;25:1109–37. doi:10.1002/(SICI)1096-9845(199610)25:10<1109::AID-EQE604>3.0.CO;2-0.
- [2] Elnashai AS, Papazoglou AJ. Procedure and spectra for analysis of rc structures subjected to strong vertical earthquake loads. vol. 1. 1997. doi:10.1080/13632469708962364.
- [3] Elgamal A, He L. Vertical earthquake ground motion records: an overview. *J Earthq Eng* 2004;8:663–97. <https://doi.org/10.1142/S1363246904001572>.
- [4] Kim SJ, Elnashai AS. seismic assessment of rc structures considering vertical ground motion by. *Mid-America Earthq Cent CD* 2008;03.
- [5] Xu Z-D, Xu F-H, Chen X. Vibration suppression on a platform by using vibration isolation and mitigation devices. *Nonlinear Dyn* 2016;83:1341–53. <https://doi.org/10.1007/s11071-015-2407-4>.
- [6] Bastián-Monarca N, Fuentes H. Errores comunes en la selección e instalación de aisladores de vibración para equipamiento mecánico en países sísmicos. *Congr. Int. Acústica y Audio Profesional* 2017.
- [7] Bastián Monarca N, Azrak I. Vibration isolation and seismic restraint for mechanical equipment in Chile. *Int Congr Acoust* 2016.
- [8] Xiongyan L, Suduo X, Yancheng C. Three-dimensional seismic isolation bearing and its application in long span hangars. *J Earthq Eng Eng Vib* 2013;12:55–65.
- [9] Xu Z-D, Tu Q, Guo Y-F. Experimental study on vertical performance of multi-dimensional earthquake isolation and mitigation devices for long-span reticulated structures. *J Vib Control* 2012;18:1971–85. <https://doi.org/10.1177/1077546311429338>.
- [10] Xu Z-D, Gai P-P, Zhao H-Y, Huang X-H, Lu L-Y. Experimental and theoretical study on a building structure controlled by multi-dimensional earthquake isolation and mitigation devices. *Nonlinear Dyn* 2017;89:723–40. <https://doi.org/10.1007/s11071-017-3482-5>.
- [11] Takahashi O, Aida H, Suhara J, Matsumoto R, Tsuyuki Y, Fujita T, et al. Construction of civil building using three dimensional seismic isolation system (Part 1, design of building using three dimensional seismic isolation system). *14th World Conf Earthq Eng* 2008.
- [12] Blom MR, Beker MG, Bertolini A, Van Den Brand JFJ, Bulten HJ, Doets M, et al. Vertical and horizontal seismic isolation performance of the advanced virgo external injection bench seismic attenuation system. *Phys Procedia* 2015;61:641–7. <https://doi.org/10.1016/j.phpro.2014.12.064>.
- [13] Shimada T, Suhara J, Inoue K. Three dimensional seismic isolation system for next-generation nuclear power plant with rolling seal type air spring and hydraulic rocking suppression system. *Am Soc Mech Eng Press Vessel Pip Div PVP* 2005;8:183–90. <https://doi.org/10.1115/PVP2005-71376>.
- [14] Inoue K, Morishita M, Fujita T. Development of three-dimensional seismic isolation technology for next generation nuclear power plant in Japan. *Am. Soc. Mech. Eng. Press. Vessel. Pip. Div. PVP*, vol. 486, 2004, p. 29–34. doi:10.1115/PVP2004-2930.
- [15] Zhou Z, Wong J, Mahin S. Potentiality of using vertical and three-dimensional isolation systems in nuclear structures. *Nucl Eng Technol* 2016;48:1237–51. <https://doi.org/10.1016/j.net.2016.03.005>.
- [16] Kageyama M, Iba T, Umeki K, Somaki T, Moro S. Development of Three Dimensional Base Isolation System with Cable Reinforcing Air Spring. *Trans. 17th Int. Conf. Struct. Mech. React. Technol. (SMIRT 17)*, 2003, p. 1–8.
- [17] Hüffmann GK. Full base isolation for earthquake protection by helical springs and viscodampers. *Nucl Eng Des* 1985;84:331–8. [https://doi.org/10.1016/0029-5493\(85\)90246-8](https://doi.org/10.1016/0029-5493(85)90246-8).
- [18] Almazán JL, Cerda FA, De la Llera JC, López-García D. Linear isolation of stainless steel legged thin-walled tanks. *Eng Struct* 2007;29:1596–611. <https://doi.org/10.1016/j.engstruct.2006.08.022>.
- [19] Alessandri S, Giannini R, Paolacci F, Malena M. Seismic retrofitting of an HV circuit breaker using base isolation with wire ropes. Part 1: Preliminary tests and analyses. *Eng Struct* 2015;98:251–62. <https://doi.org/10.1016/j.engstruct.2015.03.032>.
- [20] Alessandri S, Giannini R, Paolacci F, Amoretti M, Freddo A. Seismic retrofitting of an HV circuit breaker using base isolation with wire ropes. Part 2: Shaking-table test validation. *Eng Struct* 2015;98:263–74. <https://doi.org/10.1016/j.engstruct.2015.03.031>.
- [21] Wang W, Fang C, Zhao Y, Sause R, Hu S, Ricles J. Self-centering friction spring dampers for seismic resilience. *Earthq Eng Struct Dyn* 2019;48:1045–65. <https://doi.org/10.1002/eqe.3174>.
- [22] Riley M, Stark C, Kempner L, Mueller W. Seismic retrofit using spring damper devices on high-voltage equipment stands. *Earthq Spectra* 2006;22:733–53. <https://doi.org/10.1193/1.2216736>.
- [23] Almazán JL, Sandoval V, Gonzáles A. Dispositivo y sistema de aislación de vibraciones. *WO2013127018A1*, 2013.
- [24] García Barreneche GA. Sistema unificado para el aislamiento sísmico y aislamiento de vibraciones para. *MSc Thesis. Pontificia Universidad Católica de Chile*; 2016.
- [25] Fathali S, Filiatrault A. Experimental Seismic-Performance Evaluation of Isolation/Restraint Systems for Mechanical Equipment; Part I: Heavy Equipment Study. 2007.
- [26] González E, Almazán J, Beltrán J, Herrera R, Sandoval V. Performance of stainless steel winery tanks during the 02/27/2010 Maule Earthquake. *Eng Struct* 2013;56:1402–18. <https://doi.org/10.1016/j.engstruct.2013.07.017>.
- [27] Brunesi E, Nascimbene R, Pagani M, Beilic D. Seismic performance of storage steel tanks during the May 2012 Emilia, Italy, Earthquakes. *J Perform Constr* 2015;29:4014137. [https://doi.org/10.1061/\(ASCE\)CF.1943-5509.0000628](https://doi.org/10.1061/(ASCE)CF.1943-5509.0000628).
- [28] Rosewizk J, Kahanek C. Performance of wine storage tanks: lessons from the earthquakes near Marlborough. *Insit Stuct Eng* 2014.
- [29] Fischer EC, Liu J, Varma AH. Investigation of cylindrical steel tank damage at wineries during earthquakes: lessons learned and mitigation opportunities. *Pract Period Struct Des Constr* 2016;21:4016004. [https://doi.org/10.1061/\(ASCE\)SC.1943-5576.0000283](https://doi.org/10.1061/(ASCE)SC.1943-5576.0000283).
- [30] Auad GA, Almazán JL. Non linear vertical-rocking isolation system: application to legged wine storage tanks. *Eng Struct* 2017;152:790–803. <https://doi.org/10.1016/j.engstruct.2017.09.061>.
- [31] Praveen S, Chattopadhyay PK, Albert P, Dalvi VG, Chakraborty BC, Chattopadhyay S. Synergistic effect of carbon black and nanoclay fillers in styrene butadiene rubber matrix: development of dual structure. *Compos Part A Appl Sci Manuf* 2009;40:309–16. <https://doi.org/10.1016/j.compositesa.2008.12.008>.
- [32] Pal K, Rajasekar R, Kang DJ, Zhang ZX, Pal SK, Das CK, et al. Effect of fillers on natural rubber/high styrene rubber blends with nano silica: morphology and wear. *Mater Des* 2010;31:677–86. <https://doi.org/10.1016/j.matdes.2009.08.014>.
- [33] Fröhlich J, Niedermeier W, Luginsland HD. The effect of filler-filler and filler-elastomer interaction on rubber reinforcement. *Compos Part A Appl Sci Manuf* 2005;36:449–60. <https://doi.org/10.1016/j.compositesa.2004.10.004>.
- [34] Diani J, Fayolle B, Gilormini P. A review on the Mullins effect. *Eur Polym J* 2009;45:601–12. <https://doi.org/10.1016/j.eurpolymj.2008.11.017>.
- [35] Stoyanov AI, Natov MA. Effect of stretching on the elastic properties of polyacrylonitrile fibres. *Fibre Chem* 1980;11:464–5. <https://doi.org/10.1007/BF00547302>.
- [36] Mullins L, Tobin NR. Theoretical model for the elastic behavior of filler-reinforced vulcanized rubbers. *Rubber Chem Technol* 1957;30:555–71. <https://doi.org/10.5254/1.3542705>.
- [37] Mullins L, Tobin NR. Stress softening in rubber vulcanizates. Part I. Use of a strain amplification factor to describe the elastic behavior of filler-reinforced vulcanized rubber. *J Appl Polym Sci* 1965;9:2993–3009. <https://doi.org/10.1002/app.1965.070090906>.
- [38] Harwood JAC, Mullins L, Payne AR. Stress softening in natural rubber vulcanizates. Part II. Stress softening effects in pure gum and filler loaded rubbers. *J Appl Polym Sci* 1965;9:3011–21. <https://doi.org/10.1002/app.1965.070090907>.
- [39] Burtscher SL, Dorfmann A. Compression and shear tests of anisotropic high damping rubber bearings. *Eng Struct* 2004;26:1979–91. <https://doi.org/10.1016/j.engstruct.2004.07.014>.
- [40] Grant DN, Fenves GL, Whittaker AS. bidirectional modelling of high-damping rubber bearings. *J Earthq Eng* 2004;08:161–85. <https://doi.org/10.1142/S136324690400164X>.
- [41] Kalpakidis IV, Constantinou MC, Whittaker AS. Modeling strength degradation in lead-rubber bearings under earthquake shaking. *Earthq Eng Struct Dyn* 2010;39:1533–49. <https://doi.org/10.1002/eqe.1039>.
- [42] Lomiento G. Testing protocols for seismic isolation systems; 2011.
- [43] IEEE. IEEE Recommended Practice for Seismic Design for Substations. vol. 2005; 2006.
- [44] Charlton DJ, Yang J, Teh KK. Review of methods to characterize rubber elastic behavior for use in finite element analysis. *Rubber Chem Technol* 1994;67:481–503. <https://doi.org/10.5254/1.3538686>.
- [45] Pinarbasi S, Mengi Y. Analysis of fiber-reinforced elastomeric isolators under pure “warping” *Struct Eng Mech* 2017;61:31–47. <https://doi.org/10.12989/sem.2017.61.1.031>.
- [46] Maureira N, de la Llera J, Oyarzo C, Miranda S. A nonlinear model for multilayered rubber isolators based on a co-rotational formulation. *Eng Struct* 2017;131:1–13. <https://doi.org/10.1016/j.engstruct.2016.09.055>.
- [47] De la Llera JC, Lüders C, Leigh P, Sady H. Analysis, testing, and implementation of seismic isolation of buildings in Chile. *Earthq Eng Struct Dyn* 2004;33:543–74. <https://doi.org/10.1002/eqe.360>.
- [48] Tsai HC, Kelly JM. Stiffness analysis of fiber-reinforced rectangular seismic isolators. *J Eng Mech* 2002;128:462–70. [https://doi.org/10.1061/\(ASCE\)0733-9399\(2002\)128:4\(462\)](https://doi.org/10.1061/(ASCE)0733-9399(2002)128:4(462)).
- [49] Zhong A. “A constitutive model for the Mullins effect with permanent set in a particle-reinforced rubber” by A. Dorfmann and R.W. Ogden. *Int J Solids Struct* 2005;42:3967–9. doi:10.1016/j.ijsolstr.2004.12.002.
- [50] Elías-Zúñiga A. A phenomenological energy-based model to characterize stress-softening effect in elastomers. *Polymer (Guildf)* 2005;46:3496–506. <https://doi.org/10.1016/j.polymer.2005.02.093>.
- [51] Miñano M, Montáns FJ. A new approach to modeling isotropic damage for Mullins effect in hyperelastic materials. *Int J Solids Struct* 2015;67–68:272–82. <https://doi.org/10.1016/j.ijsolstr.2015.04.027>.
- [52] Dargazany R, Itskov M. Constitutive modeling of the Mullins effect and cyclic stress softening in filled elastomers. *Phys Rev E - Stat Nonlinear, Soft Matter Phys* 2013;88:12602. <https://doi.org/10.1103/PhysRevE.88.012602>.
- [53] Cantournet S, Desmorat R, Besson J. Mullins effect and cyclic stress softening of filled elastomers by internal sliding and friction thermodynamics model. *Int J Solids Struct* 2009;46:2255–64. <https://doi.org/10.1016/j.ijsolstr.2008.12.025>.
- [54] Rickaby SR, Scott NH. A cyclic stress softening model for the Mullins effect.pdf. *Int J Solids Struct* 2013;50:111–20.
- [55] Fernandes VA, De Focatiis DSA. The role of deformation history on stress relaxation and stress memory of filled rubber. *Polym Test* 2014;40:124–32. <https://doi.org/10.1016/j.polymertesting.2014.08.018>.
- [56] Osgooei PM, Tait MJ, Konstantinidis D. Seismic isolation of a shear wall structure using rectangular fiber-reinforced elastomeric isolators. *J Struct Eng (United States)* 2016;142. [https://doi.org/10.1061/\(ASCE\)ST.1943-541X.0001376](https://doi.org/10.1061/(ASCE)ST.1943-541X.0001376).
- [57] Bortoli DD, Wrubleski E, Marczak RJ. Hyperfit – curve fitting software for incompressible hyperelastic material models. 21st Brazilian Congr Mech Eng 2011. <https://doi.org/10.13140/2.1.4055.7448>.

- [58] Ali A. Review of constitutive models for rubber-like materials. *Am J Eng Appl Sci* 2010;3:232–9. <https://doi.org/10.3844/ajeassp.2010.232.239>.
- [59] Charalampakis AE. Parameters of Bouc-Wen hysteretic model revisited. *Proc 9th HSTAM Int Congr Mech* 2010.
- [60] Park YJ, Wen YK, Ang AH. Random vibration of hysteretic systems under bi-directional ground motions. *Earthq Eng Struct Dyn* 1986;14:543–57. <https://doi.org/10.1002/eqe.4290140405>.
- [61] McCormick J, Nagae T, Ikenaga M, Zhang PC, Katsuo M, Nakashima M. Investigation of the sliding behavior between steel and mortar for seismic applications in structures. *Earthq Eng Struct Dyn* 2009;38:1401–19. <https://doi.org/10.1002/eqe.908>.
- [62] Rabbat BG, Russell HG. Friction coefficient of steel on concrete or grout. *J Struct Eng (United States)* 1985;111:505–15. [https://doi.org/10.1061/\(ASCE\)0733-9445\(1985\)111:3\(505\)](https://doi.org/10.1061/(ASCE)0733-9445(1985)111:3(505)).
- [63] Baltay P, Gjelsvik A. Coefficient of friction for steel on concrete at high normal stress. *J Mater Civ Eng* 1990;2:46–9. [https://doi.org/10.1061/\(ASCE\)0899-1561\(1990\)2:1\(46\)](https://doi.org/10.1061/(ASCE)0899-1561(1990)2:1(46)).
- [64] Busfield JJC, Davies CKL. Stiffness of simple bonded elastomer bushes Part 1 – Initial behaviour. *Plast Rubber Compos Process Appl* 2001;30:243–57. <https://doi.org/10.1179/146580101101541679>.
- [65] Karlsson F, Persson A. Modelling Non-Linear Dynamics of Rubber Bushings n.d.
- [66] Horton JM, Gover MJC, Tupholme GE. Stiffness of rubber bush mountings subjected to radial loading. *Rubber Chem Technol* 2000;73:253–64. <https://doi.org/10.5254/1.3547589>.
- [67] Horton JM, Tupholme GE. Approximate radial stiffness of rubber bush mountings. *Mater Des* 2006;27:226–9. <https://doi.org/10.1016/j.matdes.2004.10.012>.
- [68] García Tarrago MJ. Engineering rubber bushing stiffness formulas including dynamic amplitude dependence. *Eng Sci* 2006.
- [69] García Tarrago MJ, Kari L, Vinolas J, Gil-Negrete N. Frequency and amplitude dependence of the axial and radial stiffness of carbon-black filled rubber bushings. *Polym Test* 2007;26:629–38. <https://doi.org/10.1016/j.polymertesting.2007.03.011>.
- [70] ISOVEP. ISO3D-2G isolation device 2019. <https://www.isovep.com/iso3d-2g/>.
- [71] Partom IS. Numerical calculation of equivalent moment of inertia for a fluid in a cylindrical container with partitions. *Int J Numer Methods Fluids* 1985;5:25–42. <https://doi.org/10.1002/flid.1650050104>.
- [72] Ibrahim Raouf A. *Liquid Sloshing Dynamics: Theory and Applications* 2005;vol. 1. <https://doi.org/10.1017/CBO9781107415324.004>.
- [73] Colombo JI, Almazán JL. Experimental investigation on the seismic isolation for a legged wine storage tank. *J Constr Steel Res* 2017;133:167–80. <https://doi.org/10.1016/j.jcsr.2017.02.013>.
- [74] Malhotra P. Practical nonlinear seismic analysis of tanks. *Earthq Spectra* 2000;16:473–92. <https://doi.org/10.1193/1.1586122>.
- [75] Whittaker D. Seismic design loads for storage tanks n.d.:1–7.
- [76] Psycharis IN. Effect of Base Uplift on Dynamic Response of SDOF Structures 1991;117:733–54.
- [77] Kelly TE. Tentative seismic design guidelines for rocking structures. *Bull New Zeal Soc Earthq Eng* 2009;42:239–74.
- [78] Acikgoz S, Dejong MJ. The interaction of elasticity and rocking in flexible structures allowed to uplift. *Earthq Eng Struct Dyn* 2012;41:2177–94. <https://doi.org/10.1002/eqe.2181>.
- [79] Makris N, Vassiliou MF. Are some top-heavy structures more stable? *J Struct Eng (United States)* 2014;140:1–5. [https://doi.org/10.1061/\(ASCE\)ST.1943-541X.0000933](https://doi.org/10.1061/(ASCE)ST.1943-541X.0000933).
- [80] Vassiliou MF, Mackie KR, Stojadinović B. Dynamic response analysis of solitary flexible rocking bodies: Modeling and behavior under pulse-like ground excitation. *Earthq Eng Struct Dyn* 2014;43:1463–81. <https://doi.org/10.1002/eqe.2406>.
- [81] Humrickhouse PW, Sharpe JP, Corradini ML. Comparison of hyperelastic models for granular materials. *Phys Rev E – Stat Nonlinear, Soft Matter Phys* 2010;81:835–58. <https://doi.org/10.1103/PhysRevE.81.011303>.